

Fully dynamic seismic cycle simulations in co-evolving fault damage zones controlled by damage rheology

Peng Zhai¹, Yihe Huang¹, Chao Liang² and Jean-Paul Ampuero³

¹*Earth and Environmental Sciences Department, University of Michigan–Ann Arbor, Ann Arbor, 48105, United States of America. E-mail: pengzhai@umich.edu*

²*Institute for Disaster Management and Reconstruction (IDMR), Sichuan University–The Hong Kong Polytechnic University, Chengdu, 610200, China. E-mail: chao.liang@scu.edu.cn*

³*Université Côte d'Azur, IRD, CNRS, Observatoire de la Côte d'Azur, Géoazur, Valbonne, 06560, France.*

Accepted 2025 July 16. Received 2025 July 15; in original form 2025 March 18

SUMMARY

Both short-term coseismic off-fault damage and long-term fault growth during interseismic periods have been suggested to contribute to the formation and evolution of fault damage zones. Most previous numerical models focus on simulating either off-fault damage in a single earthquake or off-fault plasticity in seismic cycles ignoring changes of elastic moduli. Here, we developed a new method to simulate the damage evolution of fault zones and dynamic earthquake cycles together in a 2-D antiplane model. We assume fault slip is governed by the laboratory-derived rate-and-state friction law while the constitutive response of adjacent off-fault material is controlled by a simplified version of the Lyakhovsky–Ben–Zion continuum brittle damage model. This study aims to present this newly developed modelling framework which opens a window to simulate the co-evolution of earthquakes and fault damage zones. We also demonstrate one example application of the modelling framework. The example simulation generates coseismic velocity drop as evidenced by seismological observations and a long-term shallow slip deficit. In addition, the coseismic slip near the surface is smaller due to off-fault inelastic deformation and results in a larger coseismic slip deficit. Here, we refer to off-fault damage as both rigidity reduction and inelastic deformation of the off-fault medium. We find off-fault damage in our example simulation mainly occurs during earthquakes and concentrates at shallow depths as a flower structure, in which a distributed damage area surrounds a localized, highly damaged inner core. With the experimentally based logarithmic healing law, coseismic off-fault rigidity reduction cannot heal fully and permanently accumulates over multiple seismic cycles. The fault zone width and rigidity eventually saturate at long cumulative slip, reaching a mature state without further change.

Key words: Elasticity and anelasticity; Numerical modelling; Seismic cycle; Earthquake dynamics; Rheology and friction of fault zones; Transform faults..

1 INTRODUCTION

1.1 Co-evolution of fault damage zone and earthquakes

Fault zone co-evolves with fault slip over multiple seismic cycles (Faulkner *et al.* 2011; Preuss *et al.* 2019). Both major strike-slip faults and subduction interfaces are surrounded by fault damage zones (Chester & Logan 1986; Chester *et al.* 1993; Caine *et al.* 1996; Ben-Zion & Sammis 2003; Rowe *et al.* 2013; Huang *et al.* 2025). Field measurements show that fracture density and inelastic strain decrease rapidly with distance from the fault core (Anders & Wiltschko 1994; Shipton & Cowie 2001; Chester *et al.* 2005; Mitchell & Faulkner 2009; Savage & Brodsky 2011; Scott *et al.*

2018; Rodriguez Padilla *et al.* 2022), suggesting that most damage occurs within a zone that is tens-to-hundreds of meters wide. The concentration of microfractures as a function of distance from the fault matches the power-law decay of seismicity away from major faults in California (Hauksson 2010), suggesting that seismicity and fault damage zone are spatially associated. In addition, the width of the damage zone increases with cumulative slip but eventually reaches a saturation (Faulkner *et al.* 2011; Savage & Brodsky 2011; Torabi *et al.* 2020).

Stress concentration due to fault slip causes damage accumulation by loading the adjacent material beyond its yielding limit. The long-term cumulative damage surrounding fault zones results from various stress concentration mechanisms operating over different

timescales. Both short-term coseismic off-fault damage associated with rupture propagation, as evidenced by pulverized rocks (Dor *et al.* 2006; Rempé *et al.* 2013), and long-term fault zone growth during the interseismic loading period (Cowie & Scholz 1992; Childs *et al.* 2009; Lyakhovsky & Ben-Zion 2009; Faulkner *et al.* 2011) have been suggested to contribute to fault zone formation and evolution. The cumulative damage occurring over multiple timescales contributes to the development of fault zone structure from an immature fault zone to a more localized mature fault zone (Chester *et al.* 1993; Ben-Zion & Sammis 2003; Mitchell & Faulkner 2009; Perrin *et al.* 2016).

1.2 Properties of fault damage zones constrained by geophysical observations

In geophysical observations, fault damage zones are manifested by low-velocity, low-rigidity zones that generate high-frequency seismic reflections (e.g. Ben-Zion *et al.* 2003) and/or anomalously high shear strain rate from geodetic observations (Chen & Freymueller 2002; Fialko *et al.* 2002; Barbot *et al.* 2009; Jolivet *et al.* 2009; Lindsey *et al.* 2014; Xu *et al.* 2020, 2023). Major fault zones are 100–400 m wide with 10–60 per cent velocity reduction, as shown by seismic imaging analysis based on trapped or guided waves (Mizuno *et al.* 2008; Lewis & Ben-Zion 2010; Eccles *et al.* 2015; Catchings *et al.* 2016; Li *et al.* 2016; Qiu *et al.* 2021), head waves (McGuire & Ben-Zion 2005; Allam *et al.* 2014; Qiu *et al.* 2023), regional tomography (Thurber *et al.* 2006; Allam & Ben-Zion 2012; Froment *et al.* 2014; White *et al.* 2021), traveltime modelling (Li *et al.* 2007; Yang *et al.* 2014), noise correlations (Hillers & Campillo 2018), controlled source seismic reflection imaging (Alaei & Torabi 2017; Alongi *et al.* 2022, 2024); as well as distributed acoustic sensing observations (Atterholt *et al.* 2022; Atterholt *et al.* 2024). Different methods lead to various depth extents of fault damage zones that range from 2–10 km. Seismically observed fault zone properties are confirmed by the borehole data of the San Andreas fault (Zoback *et al.* 2011) and the Nojima fault (Boullier *et al.* 2011) at shallow depths.

Seismic wave velocities in major fault zones are also observed to decrease after large earthquakes, a manifestation of coseismic damage and then gradually recover during post-seismic and interseismic periods (Vidale & Li 2003; Li *et al.* 2006; Brenguier *et al.* 2008; Gassenmeier *et al.* 2016; Qiu *et al.* 2019; Qin *et al.* 2020; Wang *et al.* 2021). Coseismic damage is caused by the stress concentration at the rupture tip of an earthquake (Rudnicki 1980; Swanson 1992; Scholz *et al.* 1993; Ampuero & Mao 2017). During the passage of a seismic rupture, stresses exceed the yielding limit of adjacent rocks and produce a narrow damage zone with distributed opening fractures spontaneously. Subsequently, multiple mechanisms including mechanical (Brantut *et al.* 2013) and chemical processes (Aben *et al.* 2017) are responsible for the fracture closure and recovery of seismic velocity. Particularly, the temporal change of seismic velocity and associated fault zone pore pressure evolution (Qin *et al.* 2020) suggest that fluids play an important role in modulating fault zone damage evolution.

1.3 Simulating earthquake cycles in fault damage zones

Recent earthquake cycle simulations have incorporated the fault zone structure to understand its effects on earthquake nucleation, rupture propagation and recurrence patterns. Kaneko *et al.* (2011) found through fully dynamic seismic cycle simulations that a

damaged fault zone with low rigidity resulted in reduction of earthquake nucleation size and amplification of peak slip rates. With a quasi-dynamic seismic cycle model, Abdelmeguid *et al.* (2019) showed that sufficiently compliant fault zones contribute to the emergence of subsurface events, which may cause irregular earthquake recurrence patterns. Through static rupture scaling arguments and quasi-dynamic earthquake cycle simulations, Idini & Ampuero (2020) found that the (pre-existing) low-velocity fault-zone structure can promote pulse-like rupture and back-propagating fronts via quasi-static effects even without dynamic effects of reflected waves. Thakur *et al.* (2020) systematically investigated the effects of pre-existing fault damage zones on earthquake cycles and found that the presence of elastic damage leads to variability in earthquake sizes and hypocentre locations along a single fault. Nie & Barbot (2022) also demonstrated that the existence of low-rigidity fault zones altered the earthquake nucleation size and recurrence pattern using quasi-dynamic seismic cycle models. Furthermore, Thakur & Huang (2021) found that the coseismic rigidity reduction and its interseismic recovery may explain the differences of earthquake behaviour between immature and mature fault zones. The acceleration of fault deformation before major earthquakes can also induce precursory velocity changes, which significantly reduce the nucleation size of earthquakes and influence the evolution of fault stress in dynamic earthquake cycle simulations (Thakur & Huang 2024). Recently, Flores-Cuba *et al.* (2024) explored the damage zone effects on earthquake rupture thoroughly in fully dynamic seismic cycle models and revealed potentially observable signatures of damage effects on seismic slip.

Besides the above-mentioned elastic models, there have been a few numerical studies concentrating on modelling seismic cycles with off-fault inelastic deformation. Erickson *et al.* (2017) simulated dynamic change of elastic properties and off-fault plasticity with a quasi-dynamic seismic cycle model and demonstrated the importance of inelasticity on the evolution of shallow slip deficit. With a continuum mechanics-based numerical model, Preuss *et al.* (2020) simulated both earthquake ruptures and off-fault viscoelastoplastic deformation on propagating faults. They found that faults predominantly localize and grow due to aseismic deformation, but off-fault deformation is typically formed during dynamic earthquake ruptures. With a fully dynamic seismic cycle model based on a hybrid scheme, Abdelmeguid & Elbanna (2022) found that at low cohesion, off-fault plasticity may occur during aseismic slip and therefore alter the nucleation characteristics and earthquake sequence pattern. Their results emphasize the importance of off-fault long-term inelastic deformation in seismic cycle simulations. With a similar in-plane fully dynamic seismic cycle model, Tal & Faulkner (2022) explored the effects of fault roughness and earthquake ruptures on fault zone evolution and found that the extent and distribution of plasticity depend on the characteristics of fault roughness, amount of slip and the characteristics of dynamic rupture. They suggest that quasistatic slip on rough faults may dominate the early development of off-fault plasticity with small cumulative slip. Most aforementioned seismic cycle simulations with off-fault inelasticity adopt an elasto-plastic Drucker–Prager rheology, which does not account for changes of elastic properties (e.g. reduction of shear modulus and seismic wave speeds).

1.4 Simulating co-evolution of fault damage zone and earthquakes using the continuum damage model

To combine the off-fault rigidity evolution and permanent plastic deformation together in seismic cycle simulations, we adopt a

continuum damage model (CDM) which relates damage to the elastic response in an internally consistent manner (Lyakhovsky *et al.* 1997). The CDM may also include a healing mechanism supported by laboratory experiments to capture the rigidity recovery accompanied by slow deformation during interseismic periods. Moreover, Lyakhovsky *et al.* (2005) have shown that the CDM can capture main features of rate-and-state friction validated by numerous rock friction experiments. Recently, the applicability of CDM to explain the observed rock moduli change has been further verified via both laboratory experiments and wave propagation simulations (Niu *et al.* 2024).

The CDM has been successfully used to simulate the dynamic rupture of a single earthquake (Xu *et al.* 2015; Lyakhovsky *et al.* 2016; Kurzon *et al.* 2019; Zhao *et al.* 2024). Other CDM formulations have been also proposed and used in such simulations (Bhat *et al.* 2012; Thomas *et al.* 2017; Thomas & Bhat 2018; Jara *et al.* 2021; Ferry *et al.* 2024). For a longer timescale, Lyakhovsky *et al.* (2001) modelled the coupled evolution of earthquakes and faults within one earthquake cycle governed by CDM and found that the healing timescale plays an important role in the simulated seismic activity. Using a similar 3-D quasi-static seismic cycle model without dynamic seismic radiation, Finzi *et al.* (2010) studied the structural properties and deformation patterns of evolving strike-slip faults and produced realistic fault zone geometries, including step-overs and flower structures. In the following context, we will simply use the terminology ‘damage’ to represent both rigidity reduction associated with brittle fracture and the related permanent plastic deformation.

Here, we aim to simulate the co-evolution of fault damage zones and earthquakes by capturing both coseismic damage formation and subsequent interseismic healing through the implementation of the CDM in 2-D fully dynamic earthquake cycle models. We introduce the specific governing equations of fully dynamic cycle simulations in Section 2 and the numerical framework of the spectral element method in Section 3. We present the application of this framework to simulating seismic cycles in Section 4. The example simulation demonstrates that seismic cycle models with the CDM provide important physical constraints on the evolution of fault zone structure under feedback between off-fault damage and on-fault slip accumulation over multiple seismic cycles.

2 GOVERNING EQUATIONS

2.1 Constitutive response of the fault: rate-and-state friction

We consider a pre-existing fault governed by rate-and-state friction with the aging law (Dieterich 1979; Ruina 1983). The spatial-and-time-dependent shear strength on the fault is expressed as

$$\tau = -\sigma_n \left[f_0 + a \ln \frac{V}{V_0} + b \ln \frac{V_0 \theta}{D_{RS}} \right], \quad (1)$$

$$\frac{d\theta}{dt} = 1 - \frac{V\theta}{D_{RS}}, \quad (2)$$

where σ_n is the effective normal stress, V is the slip rate, f_0 is the reference steady-state friction coefficient at the reference slip rate V_0 , a and b are rate-and-state parameters, θ is the state variable often interpreted as the average age of microcontacts between two rough surfaces and D_{RS} the characteristic weakening distance for state evolution. If $a - b < 0$ the fault is velocity-weakening at steady state and can produce dynamic slip instabilities (earthquakes), whereas if $a - b > 0$ the fault is velocity strengthening at steady state and

tends to produce stable sliding and aseismic slip. The actual shear strength is given by a rate-and-state friction regularized at zero slip velocity (Text S1, Supporting Information). Even though eqs (1) and (2) are derived from low-velocity friction experiments, they behave similarly to linear slip-weakening friction at coseismic slip rates (Cocco & Bizzarri 2002). For simplicity, here we exclude the enhanced dynamic weakening at high slip rates (Di Toro *et al.* 2004; Rice 2006; Noda *et al.* 2009).

2.2 Constitutive response of off-fault material: damage rheology

2.2.1 A modified damage rheology framework for 2-D antiplane deformation

To simulate the fracturing process of the rocks surrounding the fault using continuum mechanics, we adopt a modified version of the original continuum damage model introduced by Lyakhovsky *et al.* (1997) (Text S2, Supporting Information). The following modified damage rheology framework for 2-D antiplane deformation is inspired by analytical results of a 1-D simple shear model (Lyakhovsky *et al.* 2005). For the case of a constant volumetric strain ($I_1 = \varepsilon_{kk}$), the free energy of a damaged solid becomes

$$F = \frac{\mu}{\rho} (I_2 - I_{2,cr}), \quad (3)$$

where μ is the shear modulus, ρ is the mass density, $I_2 = \varepsilon_{ij}\varepsilon_{ij}$ is the second invariant of the elastic strain tensor ε_{ij} and the critical strain invariant $I_{2,cr}$ separates states of material degradation from healing. With the relation between stress tensor, free energy and strain tensor: $\sigma_{ij} = \rho \frac{\partial F}{\partial \varepsilon_{ij}}$, we obtain the stress-strain relation:

$$\sigma_{ij} = 2\mu\varepsilon_{ij}. \quad (4)$$

The shear modulus is assumed to evolve as

$$\mu = \mu_0 (1 - \mu_r \alpha), \quad (5)$$

where α is the non-dimensional damage variable in $[0,1]$ that represents the density of small faults in a crustal domain, μ_0 is the initial shear modulus and μ_r is the maximum allowed damage ratio which ranges from 0 to 1. Thus, $\mu_0(1 - \mu_r)$ is the minimal possible shear modulus, obtained when $\alpha = 1$, and convexity of the elastic energy ($\mu > 0$) is always guaranteed with $\mu_r < 1$ given $\mu_0 > 0$.

According to thermodynamic analysis (Lyakhovsky *et al.* 1997), the damage accumulation rate is given by

$$\frac{d\alpha}{dt} = -C \frac{\partial F}{\partial \alpha}, \quad (6)$$

where C a positive coefficient describing the temporal rate of the damage process.

Substituting the free energy in eq. (6) with eqs(3) and (5) we obtain

$$\frac{d\alpha}{dt} = \frac{C}{\rho} \mu_0 \mu_r (I_2 - I_{2,cr}) = C_d (I_2 - I_{2,cr}) = C_d Y(\varepsilon), \quad (7)$$

where the rate of damage evolution is $C_d = \frac{C}{\rho} \mu_0 \mu_r$ and $Y(\varepsilon)$ is the yield function. When the yielding threshold is exceeded, $Y(\varepsilon) > 0$, damage accumulates.

The critical value $I_{2,cr}$ is time-independent and related to the yield stress by

$$I_{2,cr} = 0.5 \left[\frac{\tau_y}{\mu_0} \right]^2, \quad (8)$$

where τ_y is the yield stress of the Drucker–Prager plasticity model (Drucker & Prager 1952)

$$\tau_y = -\sigma_m \sin(\phi) + c \cos(\phi). \quad (9)$$

Here, σ_m is the mean compressive stress (negative value for compression), ϕ is the internal friction angle with internal friction coefficient $\tan(\phi)$ and c is the rock cohesion.

2.2.2 Damage-related plastic deformation

The CDM framework provides an efficient way to simulate both the brittle fracture and the resulting off-fault plastic deformation. When $Y(\varepsilon) > 0$, the plastic strain rate is proportional to the damage accumulation rate:

$$\frac{d\varepsilon_{ij}^p}{dt} = \tau_{ij} C_v \frac{d\alpha}{dt}, \quad (10)$$

$$\tau_{ij} = 2\mu (\varepsilon_{ij}^{tol} - \varepsilon_{ij}^p), \quad (11)$$

where ε_{ij}^{tol} is the total strain, ε_{ij}^p is the plastic strain. τ_{ij} is the deviatoric stress and only results from the elastic strain tensor ε_{ij} . The damage-related inelastic strain accumulation parameter $C_v = \frac{R}{\mu_0}$ is characterized by the non-dimensional value R , which is in the order of 1 and determines the seismic coupling coefficient $\chi = 1/(1 + R)$ as given by Ben-Zion & Lyakhovsky (2006). When $R = 0$ (i.e. $\chi = 1$), the model behaves elastically without inelastic energy dissipation due to plastic strain accumulation.

2.2.3 Logarithmic healing law

The CDM also allows the rigidity (i.e. shear modulus) to heal over time, which is especially important during the post-seismic period. Healing occurs when $Y(\varepsilon) < 0$. The damage healing rate (a negative value) is proportional to the exponential of the current level of damage variable α explicitly and no prescribed permanent damage is considered in this form (Lyakhovsky *et al.* 1997):

$$\frac{d\alpha}{dt} = C_1 e^{\frac{\alpha}{C_2}} Y(\varepsilon). \quad (12)$$

For simplicity, $Y(\varepsilon)$ is assumed as a constant during the short time step for healing. More details about the time step constraints will be discussed in Section 3.1. Under this assumption, the damage variable evolves as

$$\alpha = \alpha_0 - C_2 \ln \left[1 - \frac{C_1}{C_2} e^{\frac{\alpha_0}{C_2}} Y(\varepsilon) t_0 \right], \quad (13)$$

where α_0 is the damage state at the beginning of this healing period and t_0 is the time since the beginning of this healing period. Both $C_1 > 0$ and $C_2 > 0$ are constants estimated by comparing the CDM to the rate-and-state friction law, in which the static friction coefficient is found to recover logarithmically with static contact time (Dieterich 1979). Lyakhovsky *et al.* (2005) suggested that C_2 is closely related to the parameter b of rate and state friction ($b \approx 10^{-1}$, $C_2 \approx 10^{-2} - 10^{-1} \text{ s}^{-1}$), and C_1 depends on C_2 as

$$C_1 = BC_2 \frac{\exp\left(\frac{-\alpha_0}{C_2}\right)}{Y(\varepsilon)}, \quad (14)$$

where B ($\sim 1-2 \text{ s}^{-1}$) is the timescale responsible for the evolution of static friction with hold time in laboratory experiments (Dieterich 1972, 1978).

3 NUMERICAL FRAMEWORK OF THE SPECTRAL ELEMENT METHOD

A Spectral Element Method (SEM) is used to simulate seismic cycles constrained by damage rheology and rate-and-state friction. Kaneko *et al.* (2008) initially implemented in SEM the capability to simulate spontaneous earthquake ruptures on rate-and-state faults together with wave propagation. Kaneko *et al.* (2011) further incorporated an implicit solver (for quasi-static deformation) with the original explicit solver (for earthquake rupture) to simulate long-term fully dynamic (including wave-mediated effects) seismic cycles. The ability of SEM to simulate long-term seismic cycles in heterogeneous and inelastic media comes at a high-computational cost compared to more efficient methods such as the boundary element method (Lapusta *et al.* 2000). Thakur *et al.* (2020) rewrote the previous code with Julia, a high-performance programming language especially for scientific computing, and significantly improved its efficiency. Liang *et al.* (2022) incorporated the seismic cycle modeling algorithm into sem2dpack (Ampuero 2012; Ampuero *et al.* 2024), a SEM code in Fortran that has been widely used to simulate spontaneous earthquake rupture in 2-D. Building up on this work, we further developed a new numerical framework using sem2dpack to simulate seismic cycles with off-fault inelasticity controlled by a damage rheology.

3.1 Time stepping

To simulate different timescales between spontaneous earthquake rupture and aseismic slip, we alternate between a quasi-static solver and a dynamic solver. The switch between solvers is based on a maximum slip rate threshold, which correlates with the relative importance of radiated waves and the inertial terms of the governing equations (Kaneko *et al.* 2011). The slip rate threshold is $\sim 10^{-3} \text{ m s}^{-1}$ as suggested by Kaneko *et al.* (2011). For the quasi-static solver without inertial forces, an adaptive time marching is used (Lapusta *et al.* 2000). During the coseismic periods, where wave-mediated stress transfer is considered, the time step satisfies the Courant–Friedrichs–Lewy (CFL) condition (Courant *et al.* 1928).

In the damage rheology with plasticity, an intrinsic visco-plastic regularization, which helps to reduce the potential mesh dependence, is introduced through eq. (10). The stresses (or strains) are allowed to overshoot beyond the rate-independent yield surface and subsequently relax back to it over a timescale t_v . The time step must be smaller than t_v so that the stress relaxation and damage process have sufficient time resolution when plastic deformation occurs. The default adaptive time marching (Lapusta *et al.* 2000) may yield a time step larger than t_v when the plastic deformation rate is high enough. Thus, an extra constraint on the quasi-static time step is necessary and we propose to constrain the maximum allowed time step by limiting the maximum allowed damage increment $d\alpha$ within the time step, so-called $\Delta\alpha_{\max}$ (Text S3, Supporting Information). If the practical damage increment per time step is smaller than $\Delta\alpha_{\max}$, the damage variable is updated using dt given by the default adaptive time marching (Lapusta *et al.* 2000). Otherwise, dt must be further decreased before the damage variable can be updated. This time step constraint also works when $I_2 < I_{2,\text{cr}}$ and results in a small time step for healing. Thus, $Y(\varepsilon)$ can be approximated as a constant within each small healing time step and the analytical eq. (13) holds.

For the dynamic scheme, we do not apply this extra constraint because the dynamic time step constrained by the CFL condition is typically smaller than 0.01 s. However, during coseismic rupture,

Algorithm 1 Off-fault damage and healing algorithm

Require: Total element number N , current time step number n
Ensure: Computes $\mathbf{F}^{p,n}$

- 1: **for** s from 1 to N **do** # for each element
- 2: Compute σ_{trial}^n , assuming $\varepsilon^{vp,n} = \varepsilon^{vp,n-1}$ # purely elastic response
- 3: $Y_{trial}^n = I_{2,trial}^n - I_{2,cr}$ # yield function
- 4: **if** $Y_{trial}^n \leq 0$ **then**
- 5: $()^n = ()_{trial}^n$ # the trial values are adopted
- 6: $\mathbf{F}_s^{p,n} = \mathbf{F}_s^{p,n-1}$ # no update of plastic force
- 7: $\alpha^n = \alpha^{n-1} - C_2 \ln[1 - \frac{C_1}{C_2} \exp(\frac{\alpha^{n-1}}{C_2}) Y^n \Delta t]$ # logarithmic healing
- 8: $\mu = \mu_0(1 - \mu_r \alpha^n)$ # update the shear modulus
- 9: **else** # damage and plasticity generation
- 10: $\alpha^n = \alpha^{n-1} + C_d Y_{trial}^n \Delta t$ # update damage
- 11: $\mu = \mu_0(1 - \mu_r \alpha^n)$ # update the shear modulus
- 12: $\Delta \varepsilon^{vp} = \tau_{trial}^n C_v \Delta \alpha$ # calculate the plastic strain increments
- 13: $\varepsilon^{vp,n} = \varepsilon^{vp,n-1} + \Delta \varepsilon^{vp}$
- 14: $\tau^n = \tau_{trial}^n - 2\mu \Delta \varepsilon^{vp}$ # correct the deviatoric stress
- 15: $\mathbf{F}_s^{p,n} = \int \nabla L \cdot \mu \varepsilon^{vp,n} dV_s$ # plastic force at elemental level
- 16: **end if**
- 17: **end for**
- 18: $\mathbf{F}^{p,n} = A_{s=1}^N \mathbf{F}_s^{p,n}$ # assemble the global plastic force

* ∇L is the spatial gradient of Lagrange basis function for each element

t_v might become smaller than the dynamic time step if the plastic deformation rate is high due to a relatively large C_d . We currently do not consider this scenario because C_d during dynamic rupture is typically smaller than 10^{10} s^{-1} as evidenced by experimental results (Bhat *et al.* 2012). We will discuss this in detail in the parameter selection Section 4.1.5.

3.2 Dynamic and quasi-static schemes

In the 2-D (x, z) plane of Cartesian coordinate system without body forces, the governing equation of motion under antiplane strain assumption is given by

$$\rho \frac{\partial^2 u_y}{\partial t^2} = \frac{\partial \sigma_{yx}}{\partial x} + \frac{\partial \sigma_{yz}}{\partial z}, \quad (15)$$

where ρ is the material density, u_y is the displacement out of the plane, σ_{yx} and σ_{yz} are two stress components.

The dynamic scheme to simulate spontaneous earthquake rupture with rate-and-state friction was presented first by Kaneko *et al.* (2008). It requires solving the following system of equations at every time step. The discretized weak form of the equation of motion in its matrix form:

$$\mathbf{M} \ddot{\mathbf{u}} = -\mathbf{K} \mathbf{u} + \mathbf{B} \boldsymbol{\tau}, \quad (16)$$

where \mathbf{M} is the mass matrix and \mathbf{K} is the stiffness matrix. \mathbf{B} is the fault boundary matrix—a sparse rectangular matrix obtained by assembling the contributions \mathbf{B}_e from each fault boundary element. $\boldsymbol{\tau} = \boldsymbol{\tau}^{\text{tot}} - \boldsymbol{\tau}_0$ is the relative traction vector on the fault. $\boldsymbol{\tau}^{\text{tot}}$ is the total traction while $\boldsymbol{\tau}_0$ is the reference traction in the static-equilibrium state. Note that in the current algorithm, the elastic term $\mathbf{K} \mathbf{u}$ is computed by assembling contributions from each element on-the-fly, without pre-computing and storing the global stiffness matrix \mathbf{K} . Here, we write the matrix form to help readers understand our method.

The quasi-static scheme to simulate seismic cycles was implemented first by Kaneko *et al.* (2011). During periods of quasi-static deformation, we drop the inertial term in eq. (16) and obtain:

$$\mathbf{K} \mathbf{u} = \mathbf{B} \boldsymbol{\tau}. \quad (17)$$

3.3 Implementation of damage rheology response

The CDM was first implemented in sem2dpack for dynamic rupture by Ampuero *et al.* (2008) and further developed by Xu *et al.* (2015). Building up on their work, we implement the damage rheology response for seismic cycle simulations including both dynamic deformation and quasi-static deformation.

We use a return mapping algorithm to compute the visco-plastic response. The return mapping involves first integrating the elastic equations under prescribed total strain increments to obtain an elastic predictor (trial deviatoric stress). The elastically predicted stresses are then relaxed onto a suitably updated yield surface by correcting the plastic strain increments. When plastic deformation happens, the total strain is partitioned into an elastic and a plastic component in eq. (11). For quasi-static deformation, this introduces a modification to the discretized system of equations:

$$\mathbf{K} \mathbf{u} = \mathbf{B} \boldsymbol{\tau} + \mathbf{F}^p. \quad (18)$$

The visco-plasticity contribution is described using a plastic force term denoted by \mathbf{F}^p , which is computed at an elemental level and then assembled globally. The predicted plastic forces \mathbf{F}^p , which are given in Algorithm 1, are added at each quasi-static time step explicitly. Then, we follow the quasi-static time stepping algorithms presented in Kaneko *et al.* (2011) to solve the quasi-static deformation.

For the dynamic scheme, because the internal elastic forces are computed using the elastic strain (total strain minus plastic strain), the contribution of plastic forces is accounted implicitly. We follow the algorithm by Abdelmeguid & Elbanna (2022) and show the workflow in Algorithm 1.

The shear modulus is updated at each time step based on eq. (5) at an elemental level. Besides, the global stiffness matrix \mathbf{K} in eq. (18) should also be updated during quasi-static deformation. For numerical convenience, we update \mathbf{K} every 10 time steps, because no significant modulus changes can happen within only 10 time steps. The upper limit of modulus changes within 10 time steps is estimated to be 1 percent of the initial value with $\mu_r = 0.5$ and $\Delta \alpha_{\max} = 0.002$:

$$\mu_r \times \Delta \alpha_{\max} \times \text{number of time steps} = 0.5 \times 0.002 \times 10 = 0.01 \quad (19)$$

4 APPLICATION

4.1 Numerical model and parameter selection

4.1.1 Model geometry

We consider a vertical strike-slip fault in a homogeneous half-space (Fig. 1). For a simple 2-D antiplane problem, only displacement along the y -direction is considered. The 1-D fault line is embedded in a 2-D model domain. The semi-infinite model domain (48 km by 30 km) is restricted as the medium on one side of the fault ($x \geq 0$) due to symmetry. In addition to the fault boundary ($x = 0$) and free boundary ($z = 0$), the other two boundaries are absorbing boundaries (Clayton & Engquist 1977) during the dynamic deformation. We apply the following material properties: density $\rho = 2670 \text{ kg m}^{-3}$ and shear modulus $\mu = 32 \text{ GPa}$. We use an on-fault reference friction f_0 of 0.6 (Byerlee 1978) and the same value for the off-fault bulk internal friction coefficient $\tan(\phi)$. In Byerlee's experiments (on pre-existing faults), the estimated cohesion is approximately 50 MPa with normal stress larger than 200 MPa but

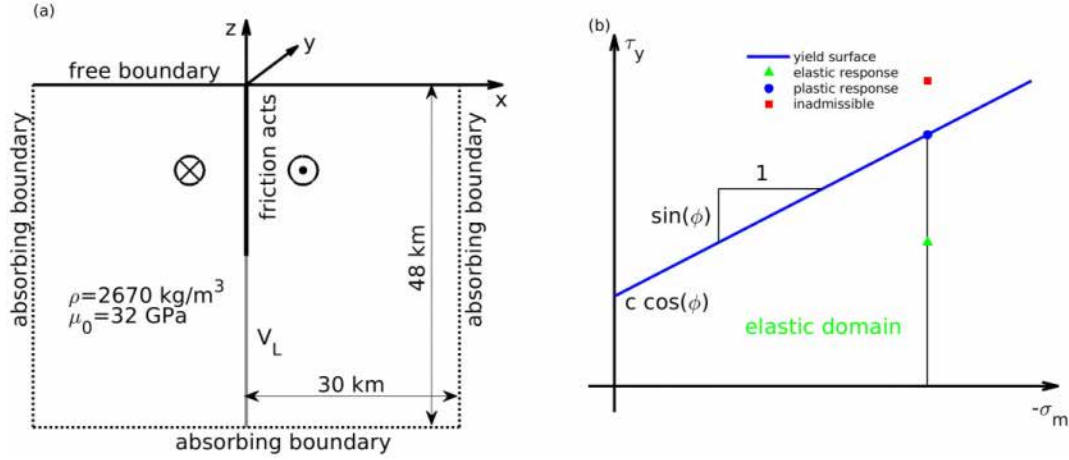


Figure 1. (a) Model geometry and (b) Drucker–Prager yielding criterion for off-fault damage. Modified from fig. 2 of Kaneko & Fialko (2011).

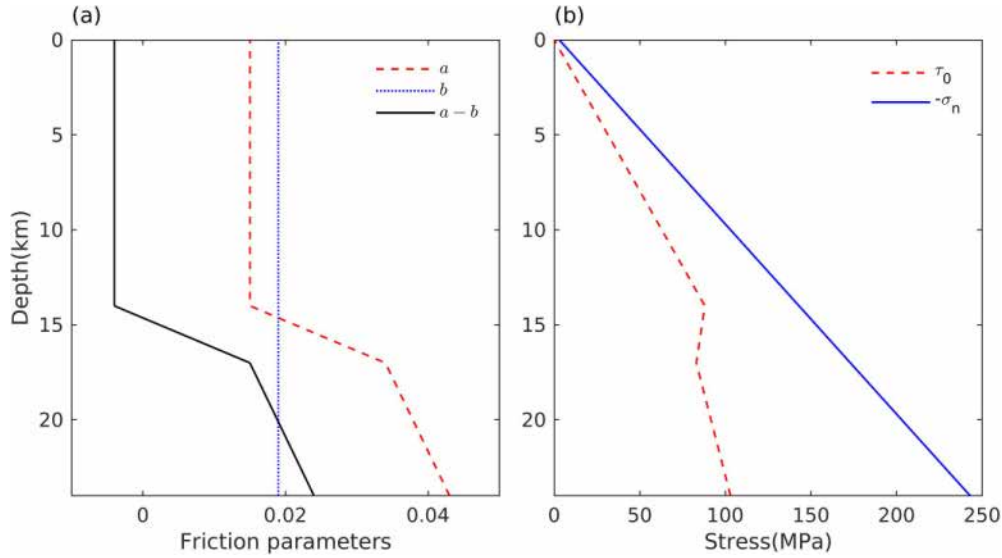


Figure 2. Depth distribution of (a) rate-and-state parameters (a , b and $a - b$), (b) absolute value of on-fault normal stress ($-\sigma_n$) and initial shear stress (τ_0).

near zero at a lower normal stress. Rock cohesion is also found to decrease as functions of plastic strain (damage) from tens of MPa to a few MPa (Zhang *et al.* 2015; Hajiabdolmajid 2017; Alidaryan *et al.* 2023). Thus, the practical rock cohesion depends on both normal stress condition and deformation process. Since the generation of fault zone damage can be inhibited by using a high-cohesion level, we simply use a constant rock cohesion c of 1 MPa to allow more damage generation and demonstrate the potential effect of fault zone damage in our example simulation. The computational domain is discretized using unstructured spectral elements with an average on-fault node-spacing of 37.5 m, which is small enough to solve the dynamic rupture on the fault (Text S4, Supporting Information). The elastic part of the seismic cycle code has been verified via a similar antiplane benchmark problem (Erickson *et al.* 2023). The results from elastic models and damage rheology models will be compared in Section 4.2.

4.1.2 Rate-and-state parameters a and b

The upper half of the fault is governed by rate-and-state friction while the lower half creeps with a constant tectonic loading rate.

The assumed distributions of rate-and-state parameters a and b with depth are shown in Fig. 2(a). They are derived from laboratory experiments (Blanpied *et al.* 1991; Blanpied *et al.* 1995) but without a shallow velocity-strengthening region, which is commonly used to generate coseismic shallow slip deficit (SSD) and post-seismic slip (after-slip) in elastic models (Lapusta *et al.* 2000). Since major earthquakes with SSD were not associated with resolvable shallow interseismic creep or robust shallow afterslip, inelastic off-fault response is considered to partially account for the existence of SSD (Kaneko & Fialko 2011). Hence, we use a pure velocity-weakening fault to isolate and understand the contribution of off-fault deformation to the generation of SSD in our simulations.

4.1.3 Stress state

The mean compressive stress is set as: $\sigma_m = -5.0 + 10.0 z$ in MPa, where z is in kilometers (negative for downward direction). The mean compressive stress used in this study (indicated by solid line in Fig. 3a) is below the hydrostatic pressure state (indicated by dash line in Fig. 3a) because of fluid overpressure in fault zone (Sibson 1994; Faulkner & Rutter 2001; Suppe 2014). The distribution

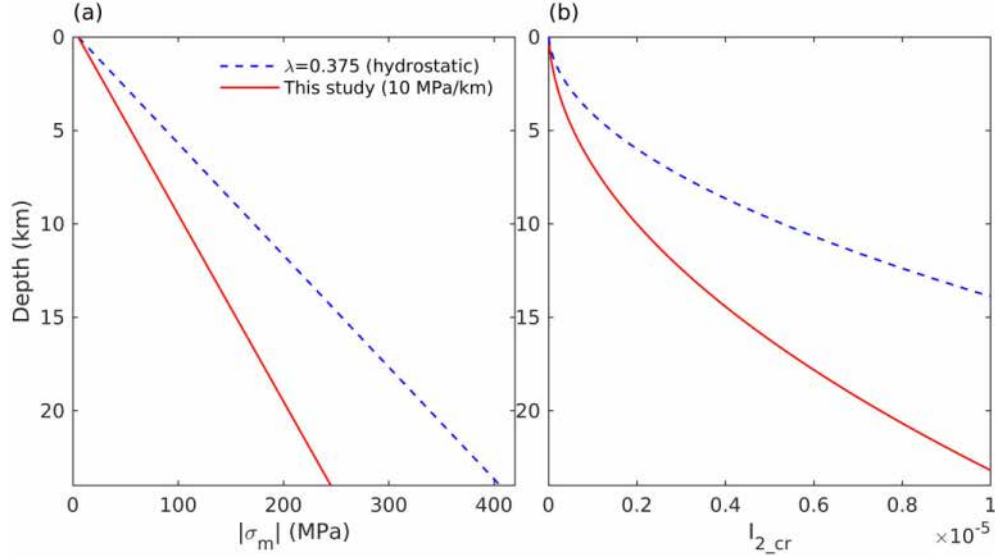


Figure 3. Depth distribution of (a) the absolute value of off-fault mean stress ($|\sigma_m|$) and (b) the corresponding $I_{2,cr}$. The hydrostatic pressure state and the related $I_{2,cr}$ (dash lines) are also plotted for reference. λ is the pore-pressure ratio, which represents the ratio between the actual fluid pressure within a rock formation and the total overburden pressure at a given depth. Thus, its value is from 0 (absence of fluid circulation) to 1 (water pressure reaches lithostatic pressure) and $\lambda = 0.375$ represents a hydrostatic pressure state.

of initial fault stresses with depth is displayed in Fig. 2(b). The effective normal stress is equal to the mean stress: $\sigma_n = \sigma_m$. An initial on-fault shear stress (indicated by dash line in Fig. 2b) is given to reduce the spin-up time (initial warming phase) in seismic cycle simulations. Besides, no extra background shear stress (or strain) exists within the computational domain at the beginning for computational convenience.

The corresponding distribution of $I_{2,cr}$ with depth is shown in Fig. 3(b). $I_{2,cr}$ increases with depth, which makes damage more difficult to generate in the deep crust. Around the seismogenic depth of the shallow crust (< 15 km), the critical second strain invariant $I_{2,cr}$ in this study (indicated by red line in Fig. 3b) is typically in the order of 10^{-6} . Note that this study focuses on the time-independent elasto-plastic deformation of the shallow crust without considering the plastic-viscous transition of the lithosphere caused by high temperature (Wang 2021).

4.1.4 Damage rheology parameters μ_r and R

The shear modulus of rocks near the surface may drop to near zero values (unconsolidated) after earthquakes. But for numerical stability, the maximum allowed damage ratio μ_r is set as 0.5 in this preliminary model. The preferred range of the damage-related inelastic strain accumulation parameter C_v is $10^{-4} - 5 \times 10^{-6} \text{ MPa}^{-1}$ based on the analysis of aftershock sequences in southern California and comparison to damage rheology predictions (Yang & Ben-Zion 2009). With the initial shear modulus $\mu_0 = 32 \text{ GPa}$ used in this study, the preferred range of the non-dimensional variable $R = \mu_0 C_v$ is 0.16–3.2. Therefore, a constant value of $R = 1$ is applied in this study.

4.1.5 Strain rate dependent C_d

Another significant damage rheology parameter is the damage rate parameter C_d , which determines the damage accumulation rate as well as the plastic deformation rate. By fitting the results of acoustic emission experiments on Darley Dale sandstone (Sammonds *et al.*

1992) and fracture experiments on Westerly granite at a similar strain rate around 10^{-5} s^{-1} , Lyakhovsky *et al.* (1997) found that the preferred range of C_d is $0.5 - 5 \text{ s}^{-1}$ but also suggested that additional constraints with different strain rates are needed. Furthermore, in order to obtain a good fit to the experimental data on Westerly granite under different confining pressures (0–1000 MPa) and loading rates ($10^{-5} - 10^{-4} \text{ s}^{-1}$), Lyakhovsky *et al.* (2005) proposed that C_d should be pressure-dependent and has a larger value ($> 10 \text{ s}^{-1}$) at shallow depth ($< 5 \text{ km}$). It should be noted that all the above experiments were conducted at small strain rates $< 10^{-4} \text{ s}^{-1}$; however, the coseismic strain rate caused by rapid fault slip may be several orders larger (e.g. $> 1 \text{ s}^{-1}$).

Based on the comparison between calculated rock strength and measured data for different rocks, Lyakhovsky *et al.* (2016) suggested that C_d should be strain rate dependent and proposed the following power-law relation:

$$\log_{10} \hat{C}_d = 1 + C_{dm} \log_{10} (\hat{\epsilon}), \quad (20)$$

where $\hat{C}_d = \frac{C_d}{C_{d0}}$ is a non-dimensional damage rate parameter normalized by $C_{d0} = 1 \text{ s}^{-1}$, C_{dm} is a constant, $\hat{\epsilon} = \frac{\dot{\epsilon}}{\dot{\epsilon}_{ref}}$ is a non-dimensional strain rate where the strain rate $\dot{\epsilon}$ is normalized by the reference value $\dot{\epsilon}_{ref} = 10^{-4} \text{ s}^{-1}$. At reference strain rate ($\hat{\epsilon} = 1$), $C_d = 10 C_{d0} = 10 \text{ s}^{-1}$. The suggested C_{dm} is 0.8.

However, there still exists a large uncertainty in the C_{dm} value suggested by Lyakhovsky *et al.* (2016) due to the scatter of laboratory data and also the lack of constraint on coseismic C_d . To get a more accurate strain rate dependence of C_d in our model, we further evaluate the two parameters C_{dm} and $\dot{\epsilon}_{ref}$ by fitting the peak stress–strain rate relation reported by Bhat *et al.* (2012). With a micromechanics based constitutive model, the simulated peak stress data under high-coseismic strain rates ($> 10^{-1} \text{ s}^{-1}$) match the experimental data on Dionysus–Pentelicon Marble well (fig. 12 in Bhat *et al.* 2012). More details about the derivation can be found in Text S5 (Supporting Information), and only the resulting quantitative relation between C_d and strain rate is reported here.

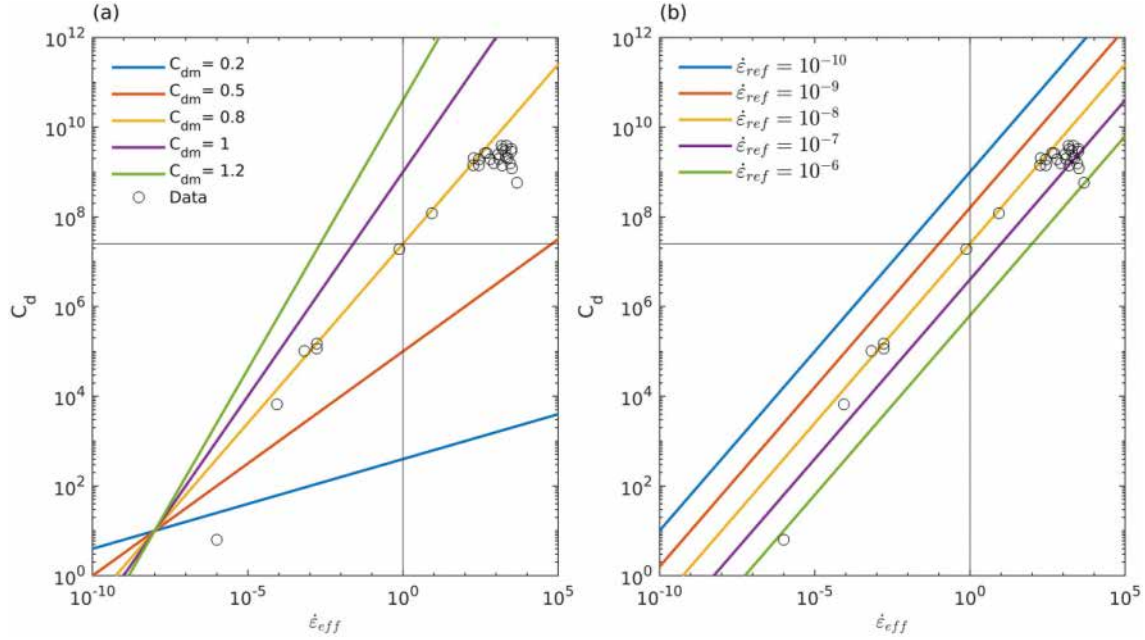


Figure 4. Damage rate parameter C_d versus effective strain rate fitted with (a) fixed reference strain rate 10^{-8} s^{-1} but different C_{dm} and (b) fixed $C_{dm} = 0.8$ but different reference strain rate. Black open circles indicate the inferred C_d based on the experimental data and simulated data extracted from (Bhat *et al.* 2012).

We find the optimized parameters are $C_{dm} = 0.8$ and $\dot{\epsilon}_{ref} = 10^{-8} \text{ s}^{-1}$ (indicated by the yellow line in Figs 4a and b). Note that to estimate the reasonable range of C_d during interseismic periods, the fitting line has been extrapolated to lower tectonic strain rates ($< 10^{-5} \text{ s}^{-1}$). Though the obtained $C_{dm} = 0.8$ is the same as previous results, the estimated $\dot{\epsilon}_{ref}$ here is 5 orders smaller than that given by Lyakhovsky *et al.* (2016). In our multitimescale seismic cycle simulations, strain rate spans a wide range from a very low-interseismic strain rate of $\sim 10^{-10} \text{ s}^{-1}$ to a high coseismic strain rate of $> 1 \text{ s}^{-1}$. Here the allowed range of C_d is from 10^{-4} to 10^7 s^{-1} compulsively for numerical stability. The maximum allowed 10^7 s^{-1} approximately corresponds to a typical coseismic strain rate of $\sim 1 \text{ s}^{-1}$ (Fig. 4).

4.1.6 Logarithmic healing parameters

The logarithmic healing law (eq. 12) is compatible with rate-and-state slide-hold-slide experiments (Dieterich 1979) where very fast healing occurs at the beginning of a hold time. As suggested by Lyakhovsky *et al.* (2005), the preferred range of C_2 is $\sim 0.01 - 0.1$, and C_1 depends on C_2 . In this study, we assume that $C_2 = 0.05$, with $B = 1 \text{ s}^{-1}$, $\alpha_0 \sim 1$, $Y(\epsilon) \sim 10^{-6}$ and it is further derived from eq. (14) that $C_1 = 10^{-4} \text{ s}^{-1}$. All key parameters used in this study are summarized in Table 1.

4.2 Results

In this section, we compare results from damage rheology models with the reference elastic model. The basic characteristics of on-fault cumulative slip and coseismic slip are displayed in Section 4.2.1. The spatial and temporal evolution of off-fault damage is presented in Section 4.2.2. More details about the temporal evolution of off-fault damage during coseismic ruptures and interseismic periods are depicted in Section 4.2.3.

4.2.1 On-fault cumulative slip

Compared with the elastic model, one important difference is that the damage rheology model has a cumulative long-term SSD over several seismic cycles. This deficit, manifested as a lag of slip in the shallow 2 km (Fig. 5b), increases with time. In other words, the fault slip in the shallow crust cannot catch up with the slip of the deeper portions of the fault in a long timescale spanning several seismic cycles. This phenomenon is also seen in previous earthquake cycle simulations with off-fault plasticity (Erickson *et al.* 2017).

The coseismic slip profiles of the elastic model and the damage rheology model are similar except at very shallow depth (shallower than 2 km), where the coseismic slip of the damage rheology model is up to 0.1 m smaller (Fig. 5c). The coseismic slip in the damage rheology model has a more significant reduction near the surface, which causes a larger coseismic SSD. This agrees with the results of Kaneko & Fialko (2011), where the contributions of off-fault plasticity on coseismic shallow slip deficit has been explored through dynamic rupture simulations of a single earthquake.

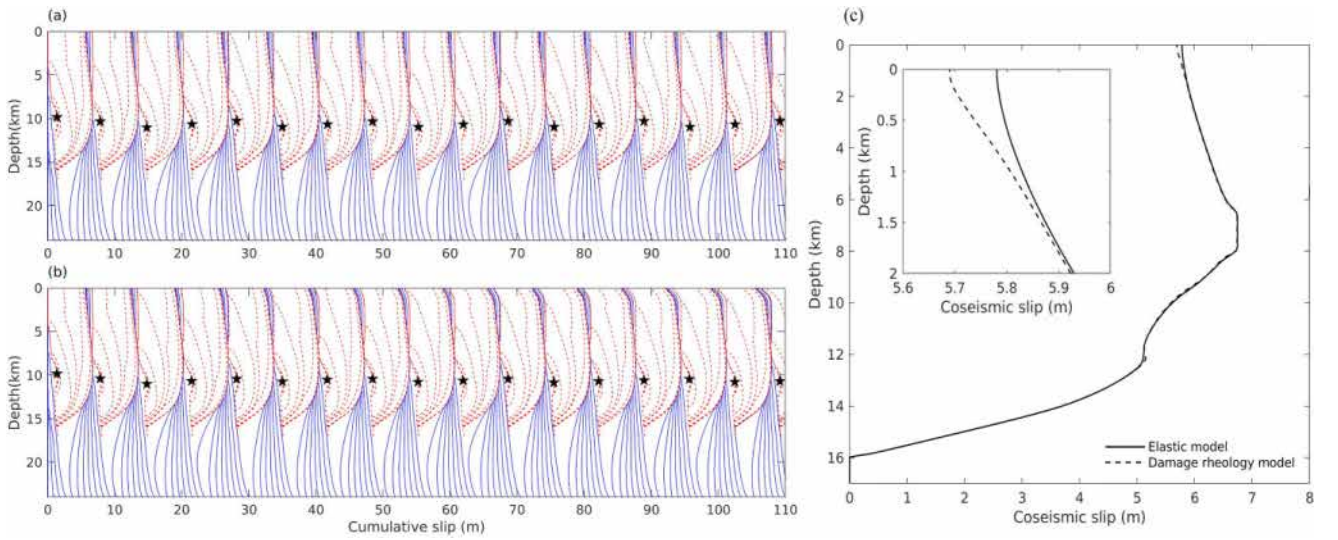
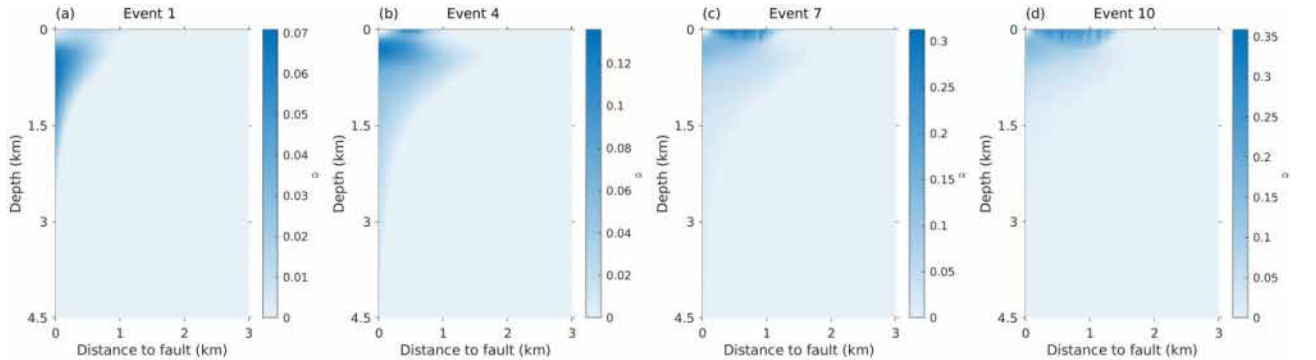
4.2.2 Off-fault damage evolution

Here the off-fault rigidity reduction is quantified by the non-dimensional damage variable α (eq. 5). The fault zone width and absolute damage variable α grows with increased cumulative fault displacement caused by repeated earthquake ruptures. From the first event to the 11th event, the maximum post-earthquake damage variable α increases from 7 per cent to over 25 per cent. The off-fault rigidity reduction pattern gradually changes from a narrow zone with a low damage level (Fig. 6a) to a wider area but with more concentrated damage near the shallow surface (Fig. 6d).

We take the off-fault damage distribution after the tenth earthquake as an example to show more details. The fault zone rigidity reduction and the related permanent plastic strain concentrate at shallow depths as a flower structure, in which a distributed damaged area surrounds a localized, highly damaged inner core (Fig. 7).

Table 1. Key parameters description

Material properties	Symbol	Value	Reference
Density (kg m^{-3})	ρ	2670	
Initial shear modulus (GPa)	μ_0	32	
On-fault friction parameters			
Reference friction coefficient	f_0	0.6	(Byerlee 1978)
Reference slip rate (m s^{-1})	V_0	10^{-6}	(Lapusta <i>et al.</i> 2000)
Direct effect, evolution effect	a, b	Variable in Fig. 2(a)	(Blanpied <i>et al.</i> 1991; Blanpied <i>et al.</i> 1995)
Characteristic weakening distance (mm)	D_{RS}	16	(Lapusta & Rice 2003)
Tectonic loading rate (m s^{-1})	V_L	10^{-9}	$\sim 30 \text{ mm yr}^{-1}$
Off-fault damage rheology parameters			
Maximum allowed damage ratio	μ_r	0.5	
Bulk internal friction coefficient	$\tan(\phi)$	0.6	(Byerlee 1978)
Rock cohesion (MPa)	c	1	
Damage accumulation rate (s^{-1})	C_d	Variable in Fig. 4	(Bhat <i>et al.</i> 2012; Lyakhovsky <i>et al.</i> 2016)
Plastic deformation ratio	R	1	(Yang & Ben-Zion 2009)
Healing parameter (s^{-1})	C_1, C_2	$10^{-4}, 0.05$	(Lyakhovsky <i>et al.</i> 2005)

**Figure 5.** Cumulative slip of (a) the elastic model and (b) the damage rheology model. The dash lines indicate the slip during coseismic rupture (every 2 s) while the solid lines are slip during the interseismic period (every 30 yr). Stars indicate the hypocentre location where the slip rate first exceeds the seismic threshold ($5 \times 10^{-3} \text{ m s}^{-1}$). (c) Depth distribution of coseismic slip averaged from the fifth event to the fifteenth event.**Figure 6.** Spatial distribution of off-fault damage variable α right after the (a) first, (b) fourth, (c) seventh and (d) eleventh earthquakes.

Within a distance of 1 km from the fault, the damage variable at the surface ($z = 0 \text{ km}$) is larger than 0.1. It attenuates rapidly as the distance to the fault increases while its attenuation along dip is slower. Like the damage variable, the permanent plastic strain

remains present at a depth up to 6 km and its half-width near the surface is $\sim 2 \text{ km}$ (Fig. 7b). The overall thickness of the fault zone, indicated by the extent of positive rigidity reduction and plastic strain, narrows with depth and stabilizes at approximately 200 to

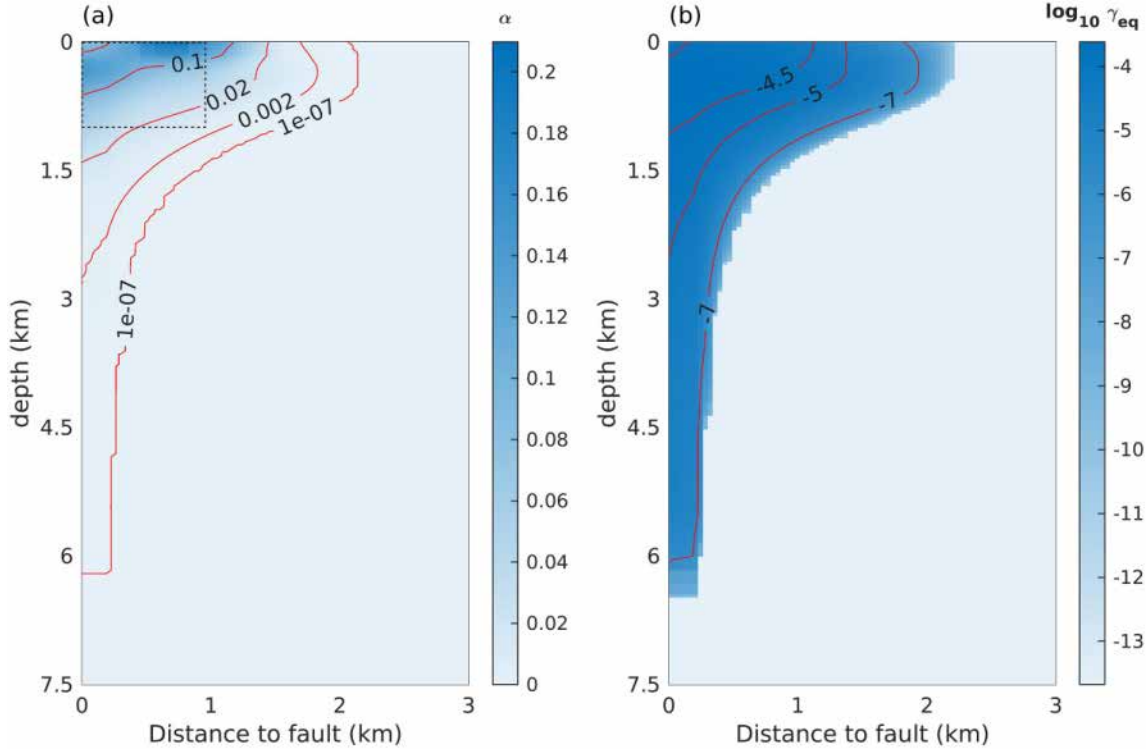


Figure 7. Spatial distribution of (a) damage variable and (b) equivalent cumulative plastic strain ($\gamma_{eq} = \sqrt{\epsilon_{ij}^p \epsilon_{ij}^p}$) after the 10th event. The grey dotted line in panel (a) represents the selected area (1 km by 1 km) to calculate the average velocity drop and the corresponding shear modulus in Fig. 8.

300 m around 6 km deep. The thickness of the spontaneously generated fault damage zone (kilometer scale at the shallower part to hundreds of meters at the deeper part) is consistent with the low-rigidity zone (or compliant zone) identified along major strike-slip faults (Unsworth *et al.* 1997; Thurber *et al.* 2003; Barbot *et al.* 2009; Lewis & Ben-Zion 2010).

To compare with seismic observations of seismic wave speed drop after major earthquakes, we calculate the spatially averaged damage evolution of a selected shallow near-fault 1 km squared area (dotted line box in Fig. 7a), and convert the rigidity reduction to the shear wave speed drop (dv/v) relative to the wave speed of the intact host rock. We find a coseismic velocity drop of around 1–2 per cent in our simulations, which approximately agrees with the values reported by seismic observations (typically a few per cent) (Vidale & Li 2003; Li *et al.* 2006; Brenguier *et al.* 2008; Gassenmeier *et al.* 2016; Qiu *et al.* 2019; Qin *et al.* 2020; Wang *et al.* 2021). The coseismic velocity drop heals only partially in the initial earthquake cycles, leaving a permanent reduction after each earthquake, which leads to a long-term fault zone growth from an immature fault zone to a low-rigidity mature fault zone.

For the set of parameters used in the damage rheology models, the fault zone rigidity saturates to a relatively stable level after ~ 7 events (i.e. 1500 yr). This is in line with the reality that the fault zone rigidity cannot keep decreasing and should approach a stabilized mature state (Mitchell & Faulkner 2009; Savage & Brodsky 2011). However, the final saturated velocity drop in this model is small (~ 2.5 per cent). A slower healing rate may cause a larger saturated velocity drop and deserves a further investigation of parameter space, which is out of the scope of this methodology study.

4.2.3 Damage budget (interseismic versus coseismic)

We also evaluate the respective contributions of interseismic and coseismic damage to the temporal evolution of fault zone damage in our simulations. We compare the damage generated by the coseismic rupture of the eighth event and the subsequent interseismic period. The eighth event is chosen because off-fault damage evolution reaches a steady state since this event (Fig. 8). We find damage mainly occurs during seismic rupture propagation and is almost complete within 2 s (12.6 s to 14.2 s in Fig. 9a) when the rupture front passes through. The interseismic period is dominated by the healing process with increasing seismic wave speed near the fault. Most of the coseismic velocity drop heals during the first quarter of the interseismic period (difference between black and red lines in Fig. 9b). For events occurring after 1500 yr, the coseismic velocity drop of the fault zone at depth (> 1 km) heals almost completely. The final depth distribution of velocity drops at the end of the interseismic period (T: pink line with stars in Fig. 9b) serves as the beginning state of the next earthquake event.

5 DISCUSSION

5.1 Comparisons with previous earthquake model with damage rheology

The damage rheology framework has been successfully applied to simulate quasi-static seismic cycles in 3-D continuum media (Lyakhovsky *et al.* 2001; Lyakhovsky & Ben-Zion 2009; Finzi *et al.* 2010) and dynamic rupture simulations that focus on the effects of single earthquake rupture (Xu *et al.* 2015; Lyakhovsky *et al.* 2016; Zhao *et al.* 2024). However, previous earthquake models

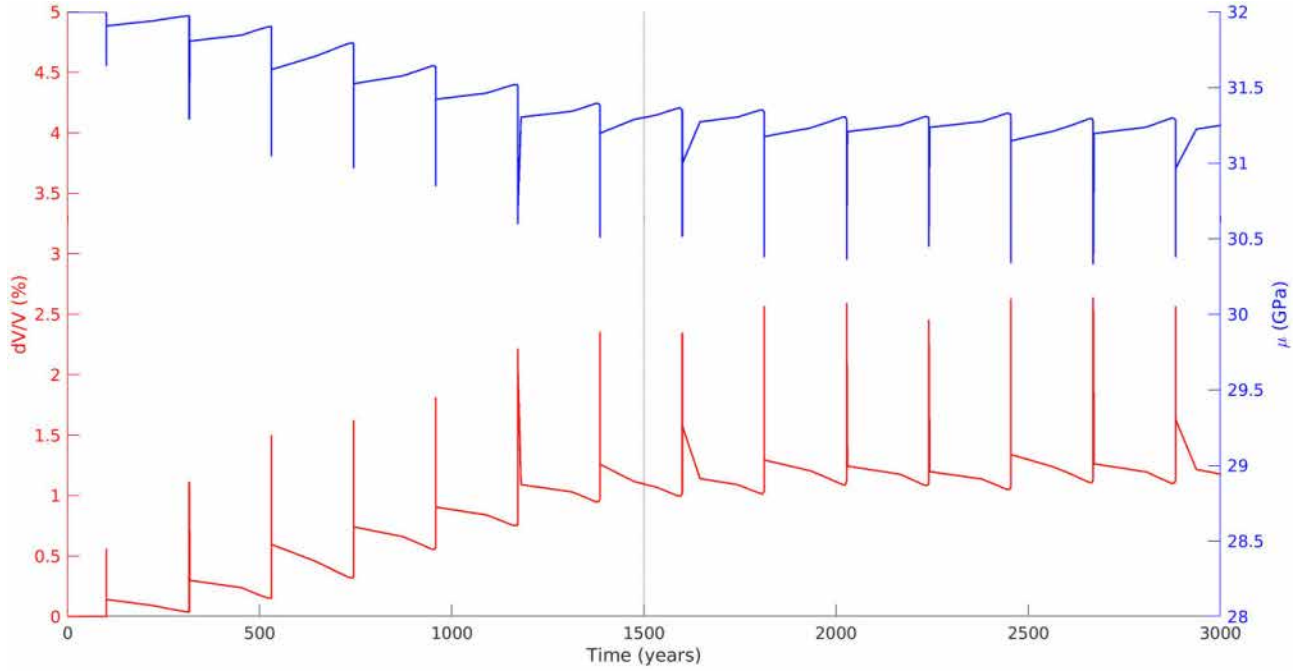


Figure 8. Shear wave velocity drop and shear modulus evolution of the 1 km squared shallow area near the fault.

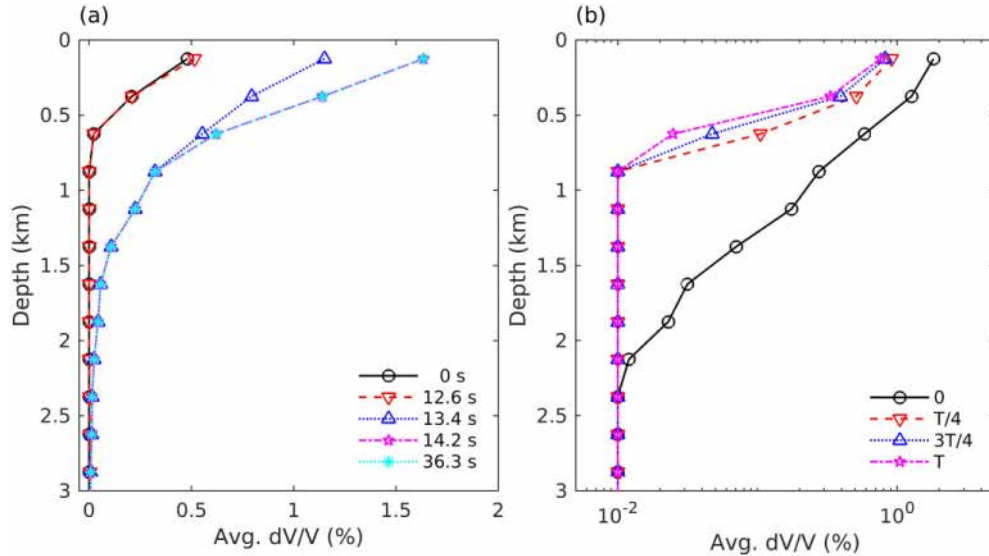


Figure 9. Depth distribution of S -wave velocity drop during (a) the coseismic phase and (b) the interseismic phase of the eighth event (dV/V less than 10^{-2} has been rounded up to 10^{-2} for a better representation with log X -axis). Different curves in panel (a) correspond to different times since earthquake onset ($t = 0$ s: beginning of the coseismic period and $t = 36.3$ s: end of the coseismic period). Different curves in panel (b) represent different interseismic stages (0: beginning of the interseismic period and T : interevent time). The velocity drop is averaged within each 0.25 km (dip direction) by 1 km (horizontal direction) rectangle near the fault.

are not able to capture both long-term earthquake recurrence and short-term dynamic earthquake rupture together in a unified model. In the quasi-static model with 3-D continuum media, only continuous deformation is simulated and there is no pre-existing fault surface where fault slip (i.e. dislocation) could happen. Thus, the quasi-static models can not explicitly simulate earthquake dynamic rupture, which is enabled by fault constitutive friction laws (e.g. rate-and-state friction). On the other hand, dynamic rupture models

only simulate single earthquake rupture without providing insights into long-term earthquake recurrence patterns.

In our multi-timescale seismic cycle simulations, fault slip is controlled by rate-and-state friction while the off-fault material evolution is governed by a damage rheology. Both the short-term coseismic rupture dynamics and long-term interseismic stress loading are captured in one single model, which contributes to a better understanding of the co-evolution of on-fault slip and off-fault damage.

Compared with seismic cycle models with only off-fault plastic deformation, the temporal evolution and spatial distribution of shear moduli (i.e. shear wave velocities) are also simulated in our models and can be directly compared with seismic observations from natural fault zones. The parameters of the damage rheology framework can also be directly estimated from laboratory experiments. For instance, the strain rate dependent C_d can be constrained by rock loading experiments as proved in Section 4.1.5 and the non-dimensional plastic deformation ratio R might be estimated through regional seismicity analysis (Yang & Ben-Zion 2009).

5.2 Mechanisms of off-fault damage generation

In our study, off-fault damage is mainly caused by the stress concentration induced by rapid propagation of the earthquake rupture tip along a pre-existing fault plane, which is called the ‘fifth model’ by Mitchell & Faulkner (2009). In contrast, the interseismic period is dominated by the recovery of fault zone rigidity. In this study, the damage budget depends on the specific value of the damage accumulation rate (C_d), which is strain rate dependent (Fig. 4). C_d takes a very high value in coseismic phase (high strain rate) but a very small value in the interseismic phase (low strain rate). Therefore, quasi-static stress concentration beyond dynamic rupture does not cause much damage and adjusting C_d could lead to different results.

This ‘fifth model’ is not in conflict with the migrating process zone model, where off-fault damage is created by the development and propagation of a ‘process zone’ around the tips of a quasi-statically growing fault (Mitchell & Faulkner 2009). They share the same mechanism that the process zone where stress concentrates, at either the rupture tip or the fault tip, leads to damage. The concept that the process zone of both earthquake ruptures and aseismic fault growth contribute to off-fault plastic yielding has been verified by simulating seismic cycles on continuum models with growing faults (Preuss *et al.* 2019; Preuss *et al.* 2020).

In addition, cumulative fault wear with increasing displacement on rough faults may facilitate off-fault damage generation (Mitchell & Faulkner 2009) and deserves further studies. Fault surface roughness caused by either geometrical complexity or heterogeneous frictional property result in off-fault damage at various scales. For example, with seismic cycle simulations on a rough fault surface, Tal & Faulkner (2022) found that the scaling of damage zone width relative to slip during quasi-static slip aligns with field observations, whereas earthquake rupture on smooth faults alone does not account for the field data. Their results suggest that quasi-static slip on rough faults plays an important role in the development of damage for small displacement faults.

5.3 Shallow slip-deficit caused by coseismic off-fault damage

In the elastic model without off-fault damage, surface slip always catches up the tectonic loading rate, whereas in the damage rheology model a long-term SSD accumulates throughout multiple seismic cycles due to the cumulative plastic strain near the surface (Fig. 5b). Coseismic SSD has been recognized by slip inversions of geodetic data from several large (magnitude ~ 7) strike-slip earthquakes, though the underlying physical mechanism remains debated. On the one hand, laboratory experiments suggested it could be caused by velocity-strengthening friction properties at shallow depth, which lead to a deficit of coseismic slip, subsequently relieved by post-seismic slip and interseismic creep. One limitation of this model is that coseismic SSD is not always

associated with significant post-seismic afterslip and interseismic creep (Fialko *et al.* 2005; Brooks *et al.* 2017; Pousse-Beltran *et al.* 2020; Wang & Bürgmann 2020). Kaneko & Fialko (2011) studied the contribution of inelastic deformation on coseismic SSD and found that the amount of shallow slip deficit is proportional to the amount of inelastic deformation near the Earth surface. With a refined slip model for the 2019 Ridgecrest, California, earthquakes, Antoine *et al.* (2024) also found that SSD positively correlates with the occurrence of diffuse deformation at the surface.

Under the framework of damage rheology, the plastic strain is associated with a spontaneously generated rigidity reduction, which can be conveniently constrained by seismological observations. It has been found that a pre-existing rigidity reduction tends to increase earthquake slip for a given stress drop (Fialko *et al.* 2002; Duan *et al.* 2011), which is in contradiction to the effects of plastic strain. One question would be the individual effects of rigidity reduction and permanent plastic strain on earthquake slip. We test two limiting cases with only either rigidity evolution ($R = 0$) or plasticity ($\mu_r = 0$) while keeping other parameters unchanged. The damage rheology model with only rigidity evolution (Fig. S8a, Supporting Information) results in nearly the same cumulative slip pattern with the reference elastic model (Fig. 5a) because a few per cent of rigidity reduction cannot alter the seismic cycle evolution significantly. On the other hand, the damage rheology model with only plasticity can still produce shallow slip deficit (Fig. S8b, Supporting Information). Therefore, our results emphasize the important contribution of inelastic strain caused by coseismic rupture on the generation of coseismic SSD in earthquake sequences. Moreover, the long-term SSD are compatible with the previous quasi-dynamic seismic cycle simulations with off-fault plasticity (Erickson *et al.* 2017) that a small amount of tectonic offset near the surface is accommodated by inelastic deformation (~ 0.1 m per rupture).

Nevertheless, a long-term decrease of fault zone rigidity will eventually alter seismic cycle evolution (Thakur *et al.* 2020; Thakur & Huang 2021). Further, we test three cases (damage rheology, rigidity evolution only and plasticity only) with a smaller healing rate, which leads to a larger rigidity reduction over tens of seismic cycles. We find that both the damage rheology model and rigidity evolution only model can have variable hypocentre locations (Fig. S9, Supporting Information) and slightly longer recurrence interval (Fig. S10, Supporting Information) compared with the plasticity only model. These results confirm that fault zone rigidity reduction can lengthen earthquake recurrence interval via amplifying earthquake slip in seismic cycle with characteristic earthquakes.

5.4 Limitations of the presented results and potential future improvements

5.4.1 2-D antiplane model controlled by a simplified CDM

In our 2-D antiplane strike-slip seismic cycle model, we only considered the shear strain evolution with the assumption of a constant volumetric strain. However, in the original damage rheology framework (Text S2, Supporting Information), the type of deformation (dilatation or contraction) governs the generation of damage where dilatation favors degradation. A relatively low shear strain could result in degradation under dilatation ($1 < \xi < \sqrt{3}$) while it only leads to healing under contraction ($-\sqrt{3} < \xi < -1$). Fault zone deformation type may also play an important role in modulating fault slip modes from stable slip to slow and fast earthquakes, as evidenced by discrete element simulations (Caniven *et al.* 2021). The original damage rheology framework can be applied to a 2-D

in-plane strain problem where the volumetric strain is not a constant. For example, in a 2-D in-plane strain dynamic rupture model with off-fault damage rheology, off-fault damage are prone to concentrate around the tensile side (Xu *et al.* 2015; Zhao *et al.* 2024).

Moreover, the damage rheology framework used in this study is modified from the classical continuum brittle damage framework (Lyakhovsky *et al.* 1997) and it does not have the representation of granular phase of elasticity, which was later incorporated into a damage-breakage model (Lyakhovsky *et al.* 2016). In future research, we plan to develop a 2-D in-plane seismic cycle model controlled by the damage-breakage rheology to further quantify the effects of deformation styles (dilatation and contraction) on long-term off-fault damage evolution over seismic cycles. We also recognize that the road to 3-D seismic cycle simulations with a comprehensive consideration of damage is methodologically and computationally challenging but necessary. With a 3-D seismic cycle model controlled by both damage rheology and rate-and-state friction, multi-scale (spatial and temporal) structural properties and deformation patterns of evolving fault zones can be better understood.

5.4.2 Single planar fault without fault roughness

Though off-fault material heterogeneity including rigidity evolution and plasticity generation have been captured by the damage rheology framework, our seismic cycle model considers a single fault, controlled by simple rate-state friction properties. In addition to material heterogeneity, natural faults have other complexities (e.g. fault roughness) that can influence slip modes as well as off-fault damage. The increase of fault roughness on natural faults may lead to larger characteristic weakening distance (D_{RS}) (Scholz 1988; Ohnaka 2003), which affects earthquake nucleation and rupture style significantly (Nie & Barbot 2022; Zhai & Huang 2024). In our model, rate-and-state friction properties are uniform in the shallow seismogenic crust. However, frictional properties on natural faults may be considerably heterogeneous due to fault roughness. Normal stress heterogeneity leads to a range of slip behaviors including system-size ruptures, widespread creep, localized slow slip as well as microseismicity (Cattania & Segall 2021) while heterogeneity of rate-and-state friction parameter ($a - b$) could explain the temporal decrease of the Gutenberg–Richter b -value prior to a large earthquake (Ito & Kaneko 2023).

Fault roughness also includes geometric irregularities in addition to frictional heterogeneity. It was found that extra shear resistance in addition to friction resistance can be introduced by fault roughness on geometrically complex faults (Fang & Dunham 2013). The geometrical complexity of fault surfaces complicates the earthquake nucleation process (Tal *et al.* 2018), modulates the evolution and scaling of fault damage zones (Tal & Faulkner 2022) and gives rise to both slow slip events and fast earthquakes (Romanet *et al.* 2018). In laboratory experiments, fault roughness promotes aftershock-like clustering (Goebel *et al.* 2023), controls slip instability (Harbord *et al.* 2017; Morad *et al.* 2022) and may be an indicator for earthquake nucleation potential (Eijsink *et al.* 2022).

Real-world faults are additionally complex because they are often part of networks of faults. The pivotal effects of the complexity of fault networks, such as bends, branches, gaps and stepovers on earthquake rupture process have been revealed by both numerical models (Harris & Day 1999; Poliakov *et al.* 2002; Bhat *et al.* 2007; Li & Liu 2020; Jia *et al.* 2023; Okuwaki *et al.* 2023) and field observations (Chu *et al.* 2021; Gauriau & Dolan 2021). Particularly, a detailed investigation of the link between fault-network geometry

and surface creep rates in California reveals that surface fault traces of creeping regions tend to be simple, whereas locked regions tend to be more complex and indicates that geometrical locking resulted from complex fault-network may promote earthquakes behaviours (Lee *et al.* 2024).

5.4.3 Parameter choice

In this study, only one single parameter choice is adopted to show that we have successfully incorporated damage rheology into fully dynamic seismic cycle simulations. However, practical physical parameters may vary a lot on natural fault zones and alter the seismic cycle evolution significantly. Previous studies have shown that the closeness to failure modulates model behaviors (Abdelmeguid & Elbanna 2022; Mia *et al.* 2022, 2023; Abdelmeguid *et al.* 2024). For example, Abdelmeguid *et al.* (2024) found that a lower cohesion (i.e. weaker fault zone) contributes to intermittent episodes of rupture and arrest and aperiodic earthquake occurrences. In our simplified version of damage rheology, the yielding threshold ($I_{2,cr}$) is fully determined by four parameters: initial shear modulus (μ_0), internal friction angle (ϕ), cohesion (c) and mean stress (σ_m) as shown in eqs (8) and (9). Any change of these parameters would alter the closeness to failure as well as the interplay between fault slip and bulk material deformation. For instance, a low internal friction coefficient (e.g. 0.2) reduces the off-fault material yielding threshold and causes complex cascading seismic events (Fig. S11, Supporting Information).

It has been found that coseismic SSD and off-fault inelastic deformation are sensitive to the quality of the fractured rock mass inside the fault damage zone in dynamic rupture models (Roten *et al.* 2017). In our seismic cycle model, a highly damaged fault zone with low material strength is also expected to cause larger coseismic SSD (e.g. ~ 1 m), which could be better resolved by available geodetic observations. Moreover, the characteristic weakening distance (D_{RS}) of on-fault rate-and-state friction significantly affects earthquake nucleation style (Zhai & Huang 2024) and recurrence patterns (Barbot 2019; Cattania 2019) in elastic media and may also alter how the damage evolves during the seismic cycle controlled by damage rheology. However, a detailed parameter study is out of scope of this methodology study, and we choose to leave this for a future exploration.

6 CONCLUSION

We have developed a framework for simulating seismic cycles controlled by a continuum damage model and rate-and-state friction. We apply it to simulate antiplane seismic cycles with co-evolving fault damage zones. The new-developed fully dynamic seismic cycle model can capture the co-evolution of fault slip and off-fault material properties and may significantly deepen our understanding of fault zone evolution over seismic cycles in the future. The example simulation demonstrates that our model with rate-and-state friction and off-fault damage can generate coseismic velocity drops and subsequent recovery as evidenced by seismological observations as well as coseismic shallow slip deficit as suggested by geodetic observations. Coseismic damage resulting from our simulation tends to concentrate at shallow depths as a flower-like structure, in which a distributed damaged area surrounds a localized, highly damaged inner core.

Damage in the example simulation mainly occurs during the short-term coseismic rupture phase while the interseismic phase is

dominated by healing (i.e. rigidity recovery). With a logarithmic healing law, the fault zone rigidity reaches a relatively stable level at large cumulative slip, which may represent a mature fault zone. Our results confirm the fundamental effects of dynamic earthquake ruptures on off-fault damage generation around a pre-existing fault. Future studies can apply this modeling framework with a more systematic parameter space to understand how fault zones and fault slip co-evolve over seismic cycles. Other mechanisms such as fault growth and fault wear effects may mainly cause off-fault damage via quasi-static effects that also require further explorations.

ACKNOWLEDGMENTS

PZ and YH were supported by the National Science Foundation (Grant Award EAR-1943742). J-PA was supported by the French government through the Investments in the Future project UCAJEDI (ANR-15-IDEX-01) managed by the National Research Agency (ANR). This research was supported in part through computational resources and services provided by Advanced Research Computing at the University of Michigan, Ann Arbor.

SUPPORTING INFORMATION

Supplementary data are available at [GJIRAS](https://www.gjiras.com) online.

Please note: Oxford University Press is not responsible for the content or functionality of any supporting materials supplied by the authors. Any queries (other than missing material) should be directed to the corresponding author for the paper.

DATA AVAILABILITY

All data are generated by numerical simulations. The source code associated with the simulation cases are contained in the Github repository at https://github.com/jpampuerto/sem2dpack/tree/rate_slip_damage (Ampuero 2012; Ampuero *et al.* 2024).

REFERENCES

- Abdelmeguid, M. & Elbanna, A., 2022. Modeling sequences of earthquakes and aseismic slip (SEAS) in elasto-plastic fault zones with a hybrid finite element spectral boundary integral scheme, *J. Geophys. Res. Solid Earth*, **127**, e2022JB024548. doi:10.1029/2022JB024548.
- Abdelmeguid, M., Ma, X. & Elbanna, A., 2019. A novel hybrid finite element-spectral boundary integral scheme for modelling earthquake cycles: application to rate and state faults with low-velocity zones, *J. Geophys. Res. Solid Earth*, **124**, 12854–12881.
- Abdelmeguid, M., Mia, M.S. & Elbanna, A., 2024. On the interplay between distributed bulk plasticity and local fault slip in evolving fault zone complexity, *Geophys. Res. Lett.*, **51**, e2023GL108060. doi:10.1029/2023GL108060.
- Aben, F.M., Doan, M.-L., Gratier, J.-P. & Renard, F., 2017. Experimental postseismic recovery of fractured rocks assisted by calcite sealing, *Geophys. Res. Lett.*, **44**, 7228–7238.
- Alaei, B. & Torabi, A., 2017. Seismic imaging of fault damaged zone and its scaling relation with displacement, *Interpretation*, **5**, SP83–SP93.
- Alidaryan, M., Khosravi, M.H., Bahaaddini, M., Moosavi, M. & Roshan, H., 2023. Mobilization of cohesion and friction angle of intact rocks in the shearing process, *Rock Mech. Rock Eng.*, **56**, 8221–8233.
- Allam, A.A. & Ben-Zion, Y., 2012. Seismic velocity structures in the southern California plate-boundary environment from double-difference tomography, *Geophys. J. Int.*, **190**, 1181–1196.
- Allam, A.A., Ben-Zion, Y. & Peng, Z., 2014. Seismic imaging of a bimaterial interface along the Hayward Fault, CA, with fault zone head waves and direct P arrivals, *Pure appl. Geophys.*, **171**, 2993–3011.
- Alongi, T., Brodsky, E.E., Kluesner, J. & Brothers, D., 2022. Using active source seismology to image the Palos Verdes Fault damage zone as a function of distance, depth, and geology, *Earth planet. Sci. Lett.*, **600**, 117871.
- Alongi, T., Brodsky, E.E., Kluesner, J. & Brothers, D., 2024. Characteristics of the fault damage zone from high-resolution seismic imaging along the Palos Verdes Fault, California, *AGU Adv.*, **5**, e2023AV001155. doi:10.1029/2023AV001155.
- Ampuero, J., Ben-Zion, Y. & Lyakhovsky, V., 2008. Interaction between dynamic rupture and off-fault damage, *Seism. Res. Lett.*, **79**, 295.
- Ampuero, J.P., 2012. *SEM2DPACK, a spectral element software for 2D seismic wave propagation and earthquake source dynamic*, v2.3.8. Zenodo.
- Ampuero, J.P. *et al.* 2024. *jpampuerto/sem2dpack: SEM2DPACK v2.3.9 (SEM2DPACK.2.3.9)*. Zenodo, [software].
- Ampuero, J.P. & Mao, X., 2017. Upper limit on damage zone thickness controlled by seismogenic depth, in *Fault Zone Dynamic Processes: Evolution of Fault Properties During Seismic Rupture*, pp. 243–253, American Geophysical Union, Washington, D.C.
- Anders, M.H. & Wiltchko, D.V., 1994. Microfracturing, paleostress and the growth of faults, *J. Struct. Geol.*, **16**, 795–815.
- Antoine, S.L., Klinger, Y., Wang, K. & Bürgmann, R., 2024. Co-seismic shallow slip deficit accounted for by diffuse off-fault deformation, *Geophys. Res. Lett.*, **51**, e2024GL110798. doi:10.1029/2024GL110798.
- Atterholt, J., Zhan, Z. & Yang, Y., 2022. Fault zone imaging with distributed acoustic sensing: body-to-surface wave scattering, *J. Geophys. Res. Solid Earth*, **127**, e2022JB025052. doi:10.1029/2022JB025052.
- Atterholt, J., Zhan, Z., Yang, Y. & Zhu, W., 2024. Imaging the Garlock Fault Zone with a fiber: a limited damage zone and hidden bimaterial contrast, *J. Geophys. Res. Solid Earth*, **129**, e2024JB028900. doi:10.1029/2024JB028900.
- Barbot, S., 2019. Slow-slip, slow earthquakes, period-two cycles, full and partial ruptures, and deterministic chaos in a single asperity fault, *Tectonophysics*, **768**, 38. doi:10.1016/j.tecto.2019.228171.
- Barbot, S., Fialko, Y. & Sandwell, D., 2009. Three-dimensional models of elastostatic deformation in heterogeneous media, with applications to the Eastern California Shear Zone, *Geophys. J. Int.*, **179**, 500–520.
- Ben-Zion, Y. *et al.* 2003. A shallow fault-zone structure illuminated by trapped waves in the Karadere-Duzce branch of the North Anatolian Fault, western Turkey, *Geophys. J. Int.*, **152**, 699–717.
- Ben-Zion, Y. & Lyakhovsky, V., 2006. Analysis of aftershocks in a lithospheric model with seismogenic zone governed by damage rheology, *Geophys. J. Int.*, **165**, 197–210.
- Ben-Zion, Y. & Sammis, C.G., 2003. Characterization of fault zones, *Pure appl. Geophys.*, **160**, 677–715.
- Bhat, H.S., Olives, M., Dmowska, R. & Rice, J.R., 2007. Role of fault branches in earthquake rupture dynamics, *J. Geophys. Res. Solid Earth*, **112**, doi:10.1029/2007JB005027.
- Bhat, H.S., Rosakis, A.J. & Sammis, C.G., 2012. A Micromechanics Based Constitutive Model for Brittle Failure at High Strain Rates, *J. Appl. Mech.*, **79**, doi:10.1115/1.4005897.
- Blanpied, M.L., Lockner, D.A. & Byerlee, J.D., 1991. Fault stability inferred from granite sliding experiments at hydrothermal conditions, *Geophys. Res. Lett.*, **18**, 609–612.
- Blanpied, M.L., Lockner, D.A. & Byerlee, J.D., 1995. Frictional slip of granite at hydrothermal conditions, *J. Geophys. Res.*, **100**, 13 045–13 064.
- Boullier, A.-M., Fagereng, Å., Toy, V.G. & Rowland, J.V., 2011. Fault-zone geology: lessons from drilling through the Nojima and Chelungpu faults, in *Geology of the Earthquake Source: A Volume in Honour of Rick Sibson*, pp. 0. Geological Society of London.
- Brantut, N., Heap, M.J., Meredith, P.G. & Baud, P., 2013. Time-dependent cracking and brittle creep in crustal rocks: a review, *J. Struct. Geol.*, **52**, 17–43.

- Brenguier, F., Campillo, M., Hadziioannou, C., Shapiro, N.M., Nadeau, R.M. & Larose, E., 2008. Postseismic relaxation along the San Andreas Fault at Parkfield from continuous seismological observations, *Science*, **321**, 1478–1481.
- Brooks, B.A. *et al.* 2017. Buried shallow fault slip from the South Napa earthquake revealed by near-field geodesy, *Sci. Adv.*, **3**, e1700525, doi:10.1126/sciadv.1700525.
- Byerlee, J., 1978. Friction of Rocks, *Pure appl. Geophys.*, **116**, 615–626.
- Caine, J.S., Evans, J.P. & Forster, C.B., 1996. Fault zone architecture and permeability structure, *Geology*, **24**, 1025–1028.
- Caniven, Y., Morgan, J.K. & Blank, D.G., 2021. The role of along-fault dilatancy in fault slip behaviour, *J. Geophys. Res. Solid Earth*, **126**, e2021JB022310. doi:10.1029/2021JB022310.
- Catchings, R.D., Goldman, M.R., Li, Y.G. & Chan, J.H., 2016. Continuity of the West Napa–Franklin Fault Zone inferred from guided waves generated by earthquakes following the 24 August 2014 Mw 6.0 South Napa Earthquake, *Bull. seism. Soc. Am.*, **106**, 2721–2746.
- Cattania, C., 2019. Complex earthquake sequences on simple faults, *Geophys. Res. Lett.*, **46**, 10384–10393.
- Cattania, C. & Segall, P., 2021. Precursory slow slip and foreshocks on rough faults, *J. Geophys. Res. Solid Earth*, **126**, e2020JB020430. doi:10.1029/2020JB020430.
- Chen, Q. & Freymueller, J.T., 2002. Geodetic evidence for a near-fault compliant zone along the San Andreas Fault in the San Francisco Bay Area, *Bull. seism. Soc. Am.*, **92**, 656–671.
- Chester, Chester, F.M. & Kronenberg, A.K., 2005. Fracture surface energy of the Punchbowl fault, San Andreas system, *Nature*, **437**, 133–136.
- Chester, Evans, J.P. & Biegel, R.L., 1993. Internal structure and weakening mechanisms of the San Andreas Fault, *J. Geophys. Res. Solid Earth*, **98**, 771–786.
- Chester, F.M. & Logan, J.M., 1986. Implications for mechanical properties of brittle faults from observations of the Punchbowl fault zone, California, *Pure appl. Geophys.*, **124**, 79–106.
- Childs, C., Manzocchi, T., Walsh, J.J., Bonson, C.G., Nicol, A. & Schöpfer, M.P.J., 2009. A geometric model of fault zone and fault rock thickness variations, *J. Struct. Geol.*, **31**, 117–127.
- Chu, S.X., Tsai, V.C., Trugman, D.T. & Hirth, G., 2021. Fault interactions enhance high-frequency earthquake radiation, *Geophys. Res. Lett.*, **48**, e2021GL095271. doi:10.1029/2021GL095271.
- Clayton, R. & Engquist, B., 1977. Absorbing boundary conditions for acoustic and elastic wave equations, *Bull. seism. Soc. Am.*, **67**, 1529–1540.
- Cocco, M. & Bizzarri, A., 2002. On the slip-weakening behavior of rate- and state dependent constitutive laws, *Geophys. Res. Lett.*, **29**, 11–11-11-14.
- Courant, R., Friedrichs, K. & Lewy, H., 1928. Über die partiellen Differenzgleichungen der mathematischen Physik, *Mathematische Annalen*, **100**, 32–74.
- Cowie, P.A. & Scholz, C.H., 1992. Growth of faults by accumulation of seismic slip, *J. Geophys. Res. Solid Earth*, **97**, 11 085–11 095.
- Dieterich, J.H., 1972. Time-dependent friction in rocks, *J. Geophys. Res. (1896-1977)*, **77**, 3690–3697.
- Dieterich, J.H., 1978. Time-dependent friction and the mechanics of stick-slip, *Pure appl. Geophys.*, **116**, 790–806.
- Dieterich, J.H., 1979. Modeling of rock friction .1. Experimental results and constitutive equations, *J. geophys. Res.*, **84**, 2161–2168.
- Di Toro, G., Goldsby, D.L. & Tullis, T.E., 2004. Friction falls towards zero in quartz rock as slip velocity approaches seismic rates, *Nature*, **427**, 436–439.
- Dor, O., Ben-Zion, Y., Rockwell, T.K. & Brune, J., 2006. Pulverized rocks in the Mojave section of the San Andreas Fault Zone, *Earth Planet. Sci. Lett.*, **245**, 642–654.
- Drucker, D.C. & Prager, W., 1952. Soil mechanics and plastic analysis or limit design, *Q. Appl. Math.*, **10**, 157–165.
- Duan, B., Kang, J. & Li, Y.-G., 2011. Deformation of compliant fault zones induced by nearby earthquakes: theoretical investigations in two dimensions, *J. Geophys. Res. Solid Earth*, **116**, doi:10.1029/2010JB007826.
- Eccles, J.D., Gulley, A.K., Malin, P.E., Boese, C.M., Townend, J. & Sutherland, R., 2015. Fault Zone Guided Wave generation on the locked, late interseismic Alpine Fault, New Zealand, *Geophys. Res. Lett.*, **42**, 5736–5743.
- Eijsink, A.M., Kirkpatrick, J.D., Renard, F. & Ikari, M.J., 2022. Fault surface morphology as an indicator for earthquake nucleation potential, *Geology*, **50**, 1356–1360.
- Erickson, B.A. *et al.* 2023. Incorporating full elastodynamic effects and dipping fault geometries in community code verification exercises for Simulations of Earthquake Sequences and Aseismic Slip (SEAS), *Bull. seism. Soc. Am.*, **113**, 499–523.
- Erickson, B.A., Dunham, E.M. & Khosravifar, A., 2017. A finite difference method for off-fault plasticity throughout the earthquake cycle, *J. Mech. Phys. Solids*, **109**, 50–77.
- Fang, Z. & Dunham, E.M., 2013. Additional shear resistance from fault roughness and stress levels on geometrically complex faults, *J. Geophys. Res. Solid Earth*, **118**, 3642–3654.
- Faulkner, Mitchell, T.M., Jensen, E. & Cembrano, J., 2011. Scaling of fault damage zones with displacement and the implications for fault growth processes, *J. Geophys. Res. Solid Earth*, **116**, doi:10.1029/2010JB007788.
- Faulkner, D.R. & Rutter, E.H., 2001. Can the maintenance of overpressured fluids in large strike-slip fault zones explain their apparent weakness?, *Geology*, **29**, 503–506.
- Ferry, R., Thomas, M.Y., Bhat, H.S. & Dubernet, P., 2024. Depth dependence of coseismic off-fault damage and its effects on rupture dynamics, *J. Geophys. Res. Solid Earth*, **130**, e2024JB029787. doi:10.1029/2024JB029787.
- Fialko, Y., Sandwell, D., Agnew, D., Simons, M., Shearer, P. & Minster, B., 2002. Deformation on nearby faults induced by the 1999 Hector Mine earthquake, *Science*, **297**, 1858–1862.
- Fialko, Y., Sandwell, D., Simons, M. & Rosen, P., 2005. Three-dimensional deformation caused by the Bam, Iran, earthquake and the origin of shallow slip deficit, *Nature*, **435**, 295–299.
- Finzi, Y., Hearn, E.H., Ben-Zion, Y. & Lyakhovsky, V., 2010. Structural properties and deformation patterns of evolving strike-slip faults: numerical Simulations Incorporating Damage Rheology, in *Mechanics, Structure and Evolution of Fault Zones*, pp. 1537–1573, eds, Ben-Zion, Y. & Sammis, C., Birkhäuser Basel, Basel.
- Flores-Cuba, J., Oral, E., Idini, B., Liang, C. & Ampuero, J.P., 2024. Mechanisms and seismological signatures of rupture complexity induced by fault damage zones in fully-dynamic earthquake cycle models, *Geophys. Res. Lett.*, **51**, e2024GL108792. doi:10.1029/2024GL108792.
- Froment, B., McGuire, J.J., van der Hilst, R.D., Gouédard, P., Roland, E.C., Zhang, H. & Collins, J.A., 2014. Imaging along-strike variations in mechanical properties of the Gofar transform fault, East Pacific Rise, *J. Geophys. Res. Solid Earth*, **119**, 7175–7194.
- Gassenmeier, M., Sens-Schönfelder, C., Eulenfeld, T., Bartsch, M., Victor, P., Tilmann, F. & Korn, M., 2016. Field observations of seismic velocity changes caused by shaking-induced damage and healing due to mesoscopic nonlinearity, *Geophys. J. Int.*, **204**, 1490–1502.
- Gauriau, J. & Dolan, J.F., 2021. Relative structural complexity of plate-boundary fault systems controls incremental slip-rate behaviour of major strike-slip faults, *Geochim. Geophys. Geosyst.*, **22**, e2021GC009938. doi:10.1029/2021GC009938.
- Goebel, T.H.W., Brodsky, E.E. & Dresen, G., 2023. Fault roughness promotes earthquake-like aftershock clustering in the Lab, *Geophys. Res. Lett.*, **50**, e2022GL101241. doi:10.1029/2022GL101241.
- Hajiabdolmajid, V., 2017. Modeling brittle failure of rock, in *Rock Mechanics and Engineering*, Vol. **1**, pp. 593–621. CRC Press.
- Harbord, C.W.A., Nielsen, S.B., De Paola, N. & Holdsworth, R.E., 2017. Earthquake nucleation on rough faults, *Geology*, **45**, 931–934.
- Harris, R.A. & Day, S.M., 1999. Dynamic 3D simulations of earthquakes on En Echelon Faults, *Geophys. Res. Lett.*, **26**, 2089–2092.
- Hauksson, E., 2010. Spatial separation of large earthquakes, aftershocks, and background seismicity: analysis of interseismic and coseismic seismicity patterns in Southern California, in *Seismogenesis and Earthquake Forecasting: The Frank Evison*, Vol. **II**, pp. 125–143, eds, Savage, M. K., Rhoades, D. A., Smith, E. G. C., Gerstenberger, M. C. & Vere-Jones, D., Springer-Verlag, Berlin.

- Hilliers, G. & Campillo, M., 2018. Fault Zone Imaging from Correlations of Aftershock Waveforms, *Pure appl. Geophys.*, **175**, 2643–2667.
- Huang, Y., Ide, S., Kato, A., Yoshida, K., Jiang, C. & Zhai, P., 2025. Fault material heterogeneity controls deep interplate earthquakes, *Sci. Adv.*, **11**, eadr9353. doi:10.1126/sciadv.adr9353.
- Idini, B. & Ampuero, J.P., 2020. Fault-zone damage promotes pulse-like rupture and back-propagating fronts via quasi-static effects, *Geophys. Res. Lett.*, **47**, doi:10.1029/2020GL090736.
- Ito, R. & Kaneko, Y., 2023. Physical mechanism for a temporal decrease of the Gutenberg–Richter *b*-value prior to a large earthquake, *J. Geophys. Res. Solid Earth*, **128**, e2023JB027413. doi:10.1029/2023JB027413.
- Jara, J. et al. 2021. Signature of transition to supershear rupture speed in the coseismic off-fault damage zone, *Proc. R. Soc. A: Math. Phys. Eng. Sci.*, **477**, 20210364. doi:10.1098/rspa.2021.0364.
- Jia, Z. et al. 2023. The complex dynamics of the 2023 Kahramanmaraş, Turkey, M_w 7.8–7.7 earthquake doublet, *Science* **381**, 985–990.
- Jolivet, R., Büttrmann, R. & Houlié, N., 2009. Geodetic exploration of the elastic properties across and within the northern San Andreas Fault zone, *Earth Planet. Sci. Lett.*, **288**, 126–131.
- Kaneko, Y., Ampuero, J.P. & Lapusta, N., 2011. Spectral-element simulations of long-term fault slip: effect of low-rigidity layers on earthquake-cycle dynamics, *J. Geophys. Res. Solid Earth*, **116**, doi:10.1029/2011JB008395.
- Kaneko, Y. & Fialko, Y., 2011. Shallow slip deficit due to large strike-slip earthquakes in dynamic rupture simulations with elasto-plastic off-fault response, *Geophys. J. Int.*, **186**, 1389–1403.
- Kaneko, Y., Lapusta, N. & Ampuero, J.-P., 2008. Spectral element modeling of spontaneous earthquake rupture on rate and state faults: effect of velocity-strengthening friction at shallow depths, *J. Geophys. Res. Solid Earth*, **113**, doi:10.1029/2007JB005553.
- Kurzon, I., Lyakhovsky, V. & Ben-Zion, Y., 2019. Dynamic rupture and seismic radiation in a damage–breakage rheology model, *Pure appl. Geophys.*, **176**, 1003–1020. doi:10.1007/s00024-018-2060-1.
- Lapusta, N. & Rice, J.R., 2003. Nucleation and early seismic propagation of small and large events in a crustal earthquake model, *J. Geophys. Res. Solid Earth*, **108**, doi:10.1029/2001JB000793.
- Lapusta, N., Rice, J.R., Ben-Zion, Y. & Zheng, G.T., 2000. Elastodynamic analysis for slow tectonic loading with spontaneous rupture episodes on faults with rate- and state-dependent friction, *J. Geophys. Res. Solid Earth*, **105**, 23 765–23 789.
- Lee, J., Tsai, V.C., Hirth, G., Chatterjee, A. & Trugman, D.T., 2024. Fault-network geometry influences earthquake frictional behaviour, *Nature*, **631**, 106–110.
- Lewis, M.A. & Ben-Zion, Y., 2010. Diversity of fault zone damage and trapping structures in the Parkfield section of the San Andreas Fault from comprehensive analysis of near fault seismograms, *Geophys. J. Int.*, **183**, 1579–1595.
- Li, Y.-G., Catchings, R.D. & Goldman, M.R., 2016. Subsurface fault damage zone of the 2014 M_w 6.0 South Napa, California, earthquake viewed from fault-zone trapped waves, *Bull. seism. Soc. Am.*, **106**, 2747–2763.
- Li, Y.-G., Chen, P., Cochran, E.S., Vidale, J.E. & Burdette, T., 2006. Seismic evidence for rock damage and healing on the San Andreas fault associated with the 2004 M 6.0 Parkfield earthquake, *Bull. seism. Soc. Am.*, **96**, S349–S363.
- Li, G. & Liu, Y., 2020. Earthquake rupture through a step-over fault system: an exploratory numerical study of the Leech River Fault, Southern Vancouver Island, *J. Geophys. Res. Solid Earth*, **125**, e2020JB020059. doi:10.1029/2020JB020059.
- Li, H., Zhu, L. & Yang, H., 2007. High-resolution structures of the Landers fault zone inferred from aftershock waveform data, *Geophys. J. Int.*, **171**, 1295–1307.
- Liang, C., Ampuero, J.-P. & Pino Muñoz, D., 2022. The paucity of supershear earthquakes on large faults governed by rate and state friction, *Geophys. Res. Lett.*, **49**, e2022GL099749. doi:10.1029/2022GL099749.
- Lindsey, E.O., Sahakian, V.J., Fialko, Y., Bock, Y., Barbot, S. & Rockwell, T.K., 2014. Interseismic strain localization in the San Jacinto Fault Zone, *Pure appl. Geophys.*, **171**, 2937–2954.
- Lyakhovsky, V. & Ben-Zion, Y., 2009. Evolving geometrical and material properties of fault zones in a damage rheology model, *Geochem. Geophys. Geosyst.*, **10**, doi:10.1029/2009GC002543.
- Lyakhovsky, V., Ben-Zion, Y. & Agnon, A., 1997. Distributed damage, faulting, and friction, *J. Geophys. Res. Solid Earth*, **102**, 27 635–27 649.
- Lyakhovsky, V., Ben-Zion, Y. & Agnon, A., 2001. Earthquake cycle, fault zones, and seismicity patterns in a rheologically layered lithosphere, **106**, 4103–4120.
- Lyakhovsky, V., Ben-Zion, Y. & Agnon, A., 2005. A viscoelastic damage rheology and rate- and state-dependent friction, *Geophys. J. Int.*, **161**, 179. doi:10.1111/j.1365-246X.2005.02583.x.
- Lyakhovsky, V., Ben-Zion, Y., Ilchev, A. & Mendecki, A., 2016. Dynamic rupture in a damage-breakage rheology model, *Geophys. J. Int.*, **206**, 1126–1143.
- McGuire, J. & Ben-Zion, Y., 2005. High-resolution imaging of the Bear Valley section of the San Andreas fault at seismogenic depths with fault-zone head waves and relocated seismicity, *Geophys. J. Int.*, **163**, 152–164.
- Mia, M.S., Abdelmeguid, M. & Elbanna, A.E., 2022. Spatio-temporal clustering of seismicity enabled by off-fault plasticity, *Geophys. Res. Lett.*, **49**, e2021GL097601. doi:10.1029/2021GL097601.
- Mia, M.S., Abdelmeguid, M. & Elbanna, A.E., 2023. The spectrum of fault slip in elastoplastic fault zones, *Earth planet. Sci. Lett.*, **619**, 118 310. doi:10.1016/j.epsl.2023.118310.
- Mitchell, T.M. & Faulkner, D.R., 2009. The nature and origin of off-fault damage surrounding strike-slip fault zones with a wide range of displacements: a field study from the Atacama fault system, northern Chile, *J. Struct. Geol.*, **31**, 802–816. doi:10.1016/j.jsg.2009.05.002.
- Mizuno, T., Kuwahara, Y., Ito, H. & Nishigami, K.y., 2008. Spatial variations in fault-zone structure along the Nojima Fault, Central Japan, as inferred from borehole observations of fault-zone trapped waves, *Bull. seism. Soc. Am.*, **98**, 558–570.
- Morad, D., Sagy, A., Tal, Y. & Hatzor, Y.H., 2022. Fault roughness controls sliding instability, *Earth planet. Sci. Lett.*, **579**, 117 365. doi:10.1016/j.epsl.2022.117365.
- Nie, S. & Barbot, S., 2022. Rupture styles linked to recurrence patterns in seismic cycles with a compliant fault zone, *Earth planet. Sci. Lett.*, **591**, 117 593. doi:10.1016/j.epsl.2022.117593.
- Niu, Z., Gabriel, A.-A., Seelinger, L. & Igel, H., 2024. Modelling and quantifying parameter uncertainty of co-seismic non-classical nonlinearity in rocks, *J. Geophys. Res. Solid Earth*, **129**, e2023JB027149. doi:10.1029/2023JB027149.
- Noda, H., Dunham, E.M. & Rice, J.R., 2009. Earthquake ruptures with thermal weakening and the operation of major faults at low overall stress levels, *J. Geophys. Res. Solid Earth*, **114**, doi:10.1029/2008JB006143.
- Ohnaka, M., 2003. A constitutive scaling law and a unified comprehension for frictional slip failure, shear fracture of intact rock, and earthquake rupture, *J. Geophys. Res. Solid Earth*, **108**, doi:10.1029/2000jb000123.
- Okuwaki, R., Yagi, Y., Taymaz, T. & Hicks, S.P., 2023. Multi-scale rupture growth with alternating directions in a complex fault network during the 2023 South-Eastern Türkiye and Syria Earthquake Doublet, *Geophys. Res. Lett.*, **50**, e2023GL103480. doi:10.1029/2023GL103480.
- Perrin, C., Manighetti, I., Ampuero, J.-P., Cappa, F. & Gaudemer, Y., 2016. Location of largest earthquake slip and fast rupture controlled by along-strike change in fault structural maturity due to fault growth, *J. Geophys. Res. Solid Earth*, **121**, 3666–3685.
- Polakov, A.N.B., Dmowska, R. & Rice, J.R., 2002. Dynamic shear rupture interactions with fault bends and off-axis secondary faulting, *J. Geophys. Res. Solid Earth*, **107**, ESE 6–1–ESE 6–18.
- Pousse-Beltran, L., Nissen, E., Bergman, E.A., Cambaz, M.D., Gaudreau, É., Karasözen, E. & Tan, F., 2020. The 2020 6.8 Elazığ (Turkey) earthquake reveals rupture behaviour of the East Anatolian Fault, *Geophys. Res. Lett.*, **47**, e2020GL088136. doi:10.1029/2020GL088136.
- Preuss, S., Ampuero, J.P., Gerya, T. & van Dinther, Y., 2020. Characteristics of earthquake ruptures and dynamic off-fault deformation on propagating faults, *Solid Earth*, **11**, 1333–1360.
- Preuss, S., Herrendörfer, R., Gerya, T., Ampuero, J.-P. & van Dinther, Y., 2019. Seismic and aseismic fault growth lead to different fault orientations, *J. Geophys. Res. Solid Earth*, **124**, 8867–8889.

- Qin, L., Ben-Zion, Y., Bonilla, L.F. & Steidl, J.H., 2020. Imaging and monitoring temporal changes of shallow seismic velocities at the Garner Valley near Anza, California, following the M7.2 2010 El Mayor-Cucapah earthquake, *J. Geophys. Res. Solid Earth*, **125**, e2019JB018070. doi:10.1029/2019JB018070.
- Qiu, H., Ben-Zion, Y., Catchings, R., Goldman, M.R., Allam, A.A. & Steidl, J., 2021. Seismic imaging of the Mw 7.1 Ridgecrest Earthquake Rupture Zone from data recorded by dense linear arrays, *J. Geophys. Res. Solid Earth*, **126**, e2021JB022043. doi:10.1029/2021JB022043.
- Qiu, H., Chi, B. & Ben-Zion, Y., 2023. Internal structure of the Central Garlock Fault Zone from Ridgecrest aftershocks recorded by dense linear seismic arrays, *Geophys. Res. Lett.*, **50**, e2022GL101761. doi:10.1029/2022GL101761.
- Qiu, H., Hillers, G. & Ben-Zion, Y., 2019. Temporal changes of seismic velocities in the San Jacinto Fault zone associated with the 2016 Mw 5.2 Borrego Springs earthquake, *Geophys. J. Int.*, **220**, 1536–1554.
- Rempe, M., Mitchell, T., Renner, J., Nippess, S., Ben-Zion, Y. & Rockwell, T., 2013. Damage and seismic velocity structure of pulverized rocks near the San Andreas Fault, *J. Geophys. Res. Solid Earth*, **118**, 2813–2831.
- Rice, J.R., 2006. Heating and weakening of faults during earthquake slip, *J. Geophys. Res. Solid Earth*, **111**, doi:10.1029/2005jb004006.
- Rodriguez Padilla, A.M., Oskin, M.E., Milliner, C.W.D. & Plesch, A., 2022. Accrual of widespread rock damage from the 2019 Ridgecrest earthquakes, *Nat. Geosci.*, **15**, 222–226.
- Romanet, P., Bhat, H.S., Jolivet, R. & Madariaga, R., 2018. Fast and slow slip events emerge due to fault geometrical complexity, *Geophys. Res. Lett.*, **45**, 4809–4819.
- Roten, D., Olsen, K.B. & Day, S.M., 2017. Off-fault deformations and shallow slip deficit from dynamic rupture simulations with fault zone plasticity, *Geophys. Res. Lett.*, **44**, 7733–7742.
- Rowe, C.D., Moore, J.C., Remitti, F. & Scientists, I.E.T., 2013. The thickness of subduction plate boundary faults from the seafloor into the seismogenic zone, *Geology*, **41**, 991–994.
- Rudnicki, J.W., 1980. Fracture mechanics applied to the Earth & crust, *Annu. Rev. Earth Planet. Sci.*, **8**, 489–525.
- Ruina, A., 1983. Slip instability and state variable friction laws, *J. geophys. Res.*, **88**, 359–370.
- Sammonds, P.R., Meredith, P.G. & Main, I.G., 1992. Role of pore fluids in the generation of seismic precursors to shear fracture, *Nature*, **359**, 228–230.
- Savage, H.M. & Brodsky, E.E., 2011. Collateral damage: evolution with displacement of fracture distribution and secondary fault strands in fault damage zones, *J. Geophys. Res. Solid Earth*, **116**, doi:10.1029/2010JB007665.
- Scholz, C.H., 1988. The critical slip distance for seismic faulting, *Nature*, **336**, 761–763.
- Scholz, C.H., Dawers, N.H., Yu, J.-Z., Anders, M.H. & Cowie, P.A., 1993. Fault growth and fault scaling laws: preliminary results, *J. Geophys. Res. Solid Earth*, **98**, 21 951–21 961.
- Scott, C.P., Arrowsmith, J.R., Nissen, E., Lajoie, L., Maruyama, T. & Chiba, T., 2018. The M7 2016 Kumamoto, Japan, Earthquake: 3-D deformation along the fault and within the damage zone constrained from Differential Lidar Topography, *J. Geophys. Res. Solid Earth*, **123**, 6138–6155.
- Shipton, Z.K. & Cowie, P.A., 2001. Damage zone and slip-surface evolution over μm to km scales in high-porosity Navajo sandstone, Utah, *J. Struct. Geol.*, **23**, 1825–1844.
- Sibson, R.H., 1994. *Crustal Stress, Faulting and Fluid Flow*, Vol. **78**, pp. 69–84, Geological Society, London, Special Publications.
- Suppe, J., 2014. Fluid overpressures and strength of the sedimentary upper crust, *J. Struct. Geol.*, **69**, 481–492.
- Swanson, M.T., 1992. Fault structure, wear mechanisms and rupture processes in pseudotachylite generation, *Tectonophysics*, **204**, 223–242.
- Tal, Y. & Faulkner, D., 2022. The effect of fault roughness and earthquake ruptures on the evolution and scaling of fault damage zones, *J. Geophys. Res. Solid Earth*, **127**, e2021JB023352. doi:10.1029/2021JB023352.
- Tal, Y., Hager, B.H. & Ampuero, J.P., 2018. The effects of fault roughness on the earthquake nucleation process, *J. Geophys. Res. Solid Earth*, **123**, 437–456.
- Thakur, P. & Huang, Y., 2024. The effects of precursory velocity changes on earthquake nucleation and stress evolution in dynamic earthquake cycle simulations, *Earth planet. Sci. Lett.*, **637**, 118 727.
- Thakur, P. & Huang, Y.H., 2021. Influence of fault zone maturity on fully dynamic earthquake cycles, *Geophys. Res. Lett.*, **48**, doi:10.1029/2021GL094679.
- Thakur, P., Huang, Y.H. & Kaneko, Y., 2020. Effects of low-velocity fault damage zones on long-term earthquake behaviors on mature strike-slip faults, *J. Geophys. Res. Solid Earth*, **125**, doi:10.1029/2020JB019587.
- Thomas, M.Y. & Bhat, H.S., 2018. Dynamic evolution of off-fault medium during an earthquake: a micromechanics based model, *Geophys. J. Int.*, **214**, 1267–1280.
- Thomas, M.Y., Bhat, H.S. & Klinger, Y., 2017. Effect of brittle off-fault damage on earthquake rupture dynamics, in *Fault Zone Dynamic Processes: Evolution of Fault Properties During Seismic Rupture*, pp. 255–280. American Geophysical Union, Washington, D.C.
- Thurber, C., Roecker, S., Roberts, K., Gold, M., Powell, L. & Rittger, K., 2003. Earthquake locations and three-dimensional fault zone structure along the creeping section of the San Andreas fault near Parkfield, CA: preparing for SAFOD, *Geophys. Res. Lett.*, **30**, doi:10.1029/2002GL016004.
- Thurber, C., Zhang, H., Waldhauser, F., Hardebeck, J., Michael, A. & Eberhart-Phillips, D., 2006. Three-dimensional compressional wavespeed model, earthquake relocations, and focal mechanisms for the Parkfield, California, Region, *Bull. seism. Soc. Am.*, **96**, S38–S49.
- Torabi, A., Ellingsen, T.S.S., Johannessen, M.U., Alaei, B., Rotevatn, A. & Chiarella, D., 2020. *Fault Zone Architecture and Its Scaling Laws: Where Does the Damage Zone Start and Stop?*, Vol. **496**, pp. 99–124. Geological Society, London, Special Publications.
- Unsworth, M.J., Malin, P.E., Egbert, G.D. & Booker, J.R., 1997. Internal structure of the San Andreas fault at Parkfield, California, *Geology*, **25**, 359–362.
- Vidale, J.E. & Li, Y.-G., 2003. Damage to the shallow Landers fault from the nearby Hector Mine earthquake, *Nature*, **421**, 524–526.
- Wang, K., 2021. If not brittle: ductile, plastic, or viscous?, *Seismol. Res. Lett.*, **92**, 1181–1184.
- Wang, K. & Bürgmann, R., 2020. Co- and early postseismic deformation due to the 2019 Ridgecrest earthquake sequence constrained by Sentinel-1 and COSMO-SkyMed SAR Data, *Seismol. Res. Lett.*, **91**, 1998–2009.
- Wang, S.-Y. et al. 2021. Near-surface softening and healing in eastern Honshu associated with the 2011 magnitude-9 Tohoku-Oki Earthquake, *Nat. Commun.*, **12**, 1215. doi:10.1038/s41467-021-21418-7.
- White, M.C.A., Fang, H., Catchings, R.D., Goldman, M.R., Steidl, J.H. & Ben-Zion, Y., 2021. Detailed traveltimes tomography and seismic catalogue around the 2019 M_w 7.1 Ridgecrest, California, earthquake using dense rapid-response seismic data, *Geophys. J. Int.*, **227**, 204–227.
- Xu, Ben-Zion, Y., Ampuero, J.-P. & Lyakhovsky, V., 2015. Dynamic ruptures on a frictional interface with off-fault brittle damage: feedback mechanisms and effects on slip and near-fault motion, *Pure appl. Geophys.*, **172**, 1243–1267.
- Xu, Liu, D. & Lavier, L., 2023. Constraining fault damage zone properties from geodesy: a case study near the 2019 Ridgecrest earthquake sequence, *Geophys. Res. Lett.*, **50**, e2022GL101692. doi:10.1029/2022GL101692.
- Xu, Sandwell, D.T., Ward, L.A., Milliner, C.W.D., Smith-Konter, B.R., Fang, P. & Bock, Y., 2020. Surface deformation associated with fractures near the 2019 Ridgecrest earthquake sequence, *Science*, **370**, 605–608.
- Yang, W. & Ben-Zion, Y., 2009. Observational analysis of correlations between aftershock productivities and regional conditions in the context of a damage rheology model, *Geophys. J. Int.*, **177**, 481–490.
- Yang, H., Li, Z., Peng, Z., Ben-Zion, Y. & Vernon, F., 2014. Low-velocity zones along the San Jacinto Fault, Southern California, from body waves recorded in dense linear arrays, *J. Geophys. Res. Solid Earth*, **119**, 8976–8990.

- Zhai, P. & Huang, Y., 2024. The effects of characteristic weakening distance on earthquake nucleation styles in fully dynamic seismic cycle simulations, *J. Geophys. Res. Solid Earth*, **129**, e2024JB029719. doi:10.1029/2024JB029719.
- Zhang, H.Q., Tannant, D.D., Jing, H.W., Nunoo, S., Niu, S.J. & Wang, S.Y., 2015. Evolution of cohesion and friction angle during microfracture accumulation in rock, *Nat. Hazards*, **77**, 497–510.
- Zhao, C., Mia, M.S., Elbanna, A. & Ben-Zion, Y., 2024. Dynamic rupture modeling in a complex fault zone with distributed and localized damage, *Mech. Mater.*, **198**, 105 139.
- Zoback, M., Hickman, S. & Ellsworth, W., 2011. Scientific drilling into the San Andreas Fault Zone—an overview of SAFOD’s first five years, *Sci. Drill.*, **11**, 14–28.